Stable isotope and geochronological study of the Mawchi Sn-W deposit, Myanmar: implications for timing of mineralization and ore genesis

Aung Zaw Myint[1, 2, *], Kotaro Yonezu[2], Adrian J. Boyce[3], David Selby[4], Anders Scherstén[5], Thomas Tindell[2], Koichiro Watanabe[2], Ye Myint Swe[6]

[1]Department of Geology, University of Yangon, Yangon, Kamayut 11041, Myanmar

[2]Economic Geology Lab, Department of Earth Resources Engineering, Kyushu University, Fukuoka 819-0395, Japan

[3]Scottish Universities Environmental Research Centre (SUERC), Glasgow, G75 0QF, Scotland, United Kingdom

[4]Department of Earth Sciences, University of Durham, Durham, DH1 3LE United Kingdom

[5]Department of Geology, Lund University, 117 221 00 Lund, Sweden

[6]Department of Geological Survey and Mineral Exploration, Naypyitaw 100604, Myanmar

*corresponding author

E-mail: aungzawmyint.myanmar@gmail.com

Abstract

Myanmar is endowed with abundant Sn-W mineralization, pre-eminent amongst which is the world-class Mawchi deposit. In the Mawchi area, N-S trending vertical or steeply dipping quartz veins are hosted by both Eocene granite and Carboniferous to Early Permian metasediments. Three stages of ore formation are recognized; (i) tourmaline-cassiterite stage (ii) main ore stage and (iii) sulfide stage. Tourmaline, cassiterite and pyrite-I are early-formed minerals and are representative of the first stage. Their deposition continued together with wolframite, scheelite, molybdenite, arsenopyrite, pyrite-II, fluorite and danalite, which form the second stage. This was followed by the successive deposition of sulfides such as chalcopyrite, sphalerite, galena and Pb-Bi sulfides. A $^{40}Ar/^{39}Ar$ magmatic biotite plateau age of 41.50 ± 0.16 Ma (MSWD = 2.5) is determined for the Mawchi biotite granite which we interpret as the time the granite cooled through the biotite blocking temperature, and is consistent with a previously reported LA-ICP-MS U-Pb zircon concordia age of 42.72 ± 0.94 Ma (MSWD = 2). A molybdenite Re-Os model age of 42.4 ± 1.2 Ma indicates that Sn-W mineralization was synchronous with late Eocene granitic magmatism. Our $^{40}Ar/^{39}Ar$ hydrothermal muscovite plateau ages from the tourmaline granite (40.14 ± 0.14 Ma; MSWD = 1.48) and quartz vein selvages (40.80 ± 0.12 Ma; MSWD = 0.47) define the timing of hydrothermal alteration and simultaneous veining that accompanied the late stage of ore forming at Mawchi.

Fluid inclusion microthermometry from cassiterite, scheelite, quartz, and fluorite reveals that ore fluids in the cassiterite-tourmaline stage and main ore stage are characterized by moderate homogenization temperatures (Th = 260˚- 345˚C) and salinities (4.5 – 15.7 wt. % NaCl equiv), while the sulfide stage is characterized by lower temperatures (Th = 175˚- 260˚C) and moderate to low salinity (2.5 – 13 wt. % NaCl equiv). The mean $\delta^{34}S$ of all sulfides is 2.9 ± 2.9 ‰, which is suggestive that the overall system is dominated by magmatic sulfur. The similarity of $\delta^{34}S$ values in galena and Pb-Bi sulfides (-1.3 – 2.7 ‰) suggest that sulfur, and inference the Pb and Bi were transported by a common fluid, probably of magmatic origin. The calculated $\delta^{18}O_{H_2O}$ of the hydrothermal fluid associated with cassiterite and tourmaline is 7.3 to 8.4 ‰. Scheelite and quartz deposition is characterized by lighter $\delta^{18}O_{H_2O}$ values (2.1 to 4.9 ‰) indicating that the ore fluid might be mixed with another source of water, perhaps,

meteoric. Hydrogen isotopic compositions (δD = -51 to -121 ‰) again indicate that origin of the ore fluid is magmatic, but δD (~ -120 ‰) is low enough to support the $\delta^{18}O_{H_2O}$ data that suggests, in part, a meteoric water component to the hydrothermal fluids at Mawchi.

Keywords: Mawchi, Sn-W, stable isotope, geochronology, timing, ore genesis

1. Introduction

Myanmar is richly endowed with mineral resources and has a long history of mining for lead-zinc-silver, tin-tungsten, gold-copper and gemstones (Thein, 1991; United Nations, 1996; Gardiner et al., 2015). Tin-tungsten (Sn-W) mineralization is one of the principal mineral resources in the country with 11,000 tonnes of tin concentrate produced in 2014, accounting for 3.72% of total world production (USGS, 2015).

The Southeast Asia tin belt, extending for 2800 km in length and up to 400 km wide extends from Billiton Island, Indonesia, in the south, through Peninsula Malaysia via southern peninsula Thailand to central and northern Thailand, eastern Myanmar and Yunnan Province (China). Collectively, the four granite belts of southeast Asia (Fig. 1a) represent one of the great metallotects of the World – their metallogenic endowment is dominated by Sn-W (Eastern Granite Province, Central Granite Province and Western Granite Province), with significant Cu-Au-Mo porphyry-epithermal mineralization being a feature of the Central Valley Province.

The major tin and tungsten deposits are associated with the granites of Central Granite Province (CGP) and Western Granite Province (WGP). CGP contains the S-type granites of Triassic to Early Jurassic (Ng et al., 2015b) whereas WGP is made up of Cretaceous to Eocene I- and S-type granites (Charusiri et al., 1993; Cobbing et al., 1992; Barley et al., 2003; Mitchell et al., 2012). Mawchi deposit is located in the middle of WGP. The CGP is Indosinian in age and for

more than 40 years has been explained by a late Triassic continent- continent or continent- island arc collision consequent on the closure of Palaeo-Tethys (Mitchell, 1977; Ng et al., 2015a&b). Granites and tin mineralization in the WGP overlap in time the India- Asia collision at ca 60 Ma and ca 45 Ma but the southern end of the WGP is far from the nearest exposures of continental Indian crust in northernmost Myanmar. S-type granites in the WGP might be explicable by slab detachment beneath Myanmar- Thailand in response to the Indian collision, but a more local tectonic control related to subduction of the oceanic Indian plate seems more probable (Gardiner et al., 2015; Jiang et al., 2017).

The WGP is dominated by ilmenite-series rocks (Charusiri et al., 1993; Myint et al., 2017 a & b) of granodioritic to syenogranitic composition (Cobbing et al., 1992; Cobbing, 2011). In Thailand, the Cretaceous to Eocene (88-50Ma) granitoids of both the Sn-W bearing S-type and barren I-type granites intrude Carboniferous to Permian clastic sedimentary rocks at Phuket, Ranong and Pilok (Charusiri et al., 1993). In Myanmar, magnetite-series I-type granitic to dioritic rocks are exposed in some localities (eg. Yebokson, Yinmabin, Nattaung, Mokpalin etc.) (Cobbing et al., 1992; Barley et al., 2003; Mitchell et al., 2012) whereas highly fractionated ilmenite-seires biotite and muscovite granites are spatially associated with Sn-W mineralization in the vicinity of Padatchaung, Mawchi, Dawei, Myeik and Yadanabon areas. Available geochronological data indicates that these tin granites crystallized during Cretaceous to Eocene (107 - 42 Ma) (Brook and Snelling, 1976; Myint et al., 2013; Paik and Zaw, 2014; Gardiner et al., 2016; Myint et al.,

105 2017a&b; Li et al., under submission). In the northern segment of the Sibumasu terrane, the
106 Tengchong-Baoshan granitoid province (TBGP) hosts large- and medium-sized Sn deposits (Wang
107 et al., 2014; Chen et al., 2015). These tin granites of the Yunnan Province link to the granitoids of
108 northeastern Myanmar and emerge as the likely northern continuation of WGP. They are mostly
109 biotite granites with high silica content (73.3 - 76.2 wt.%) and, have metaluminous to weakly
110 peraluminous and high-K calcalkaline compositions. These characters resemble those of the WGP
111 tin granites. Recently LA-MC-ICP-MS U-Pb zircon ages of 53 and 73 Ma have been reported for
112 the Xiaolonghe and Lailishan tin granites, respectively (Chen et al., 2015).

113 The WGP in Myanmar has over 400 Sn-W occurrences and most of them are associated
114 with granites, granite pegmatites and aplite dykes of the WGP. Sn-W mineralization in the Tin
115 Province is found as cassiterite and/or wolframite-bearing pegmatites and greisen-bordered quartz
116 veins. These are hosted both by the granites, and also by the Slate Belt country rock. Among the
117 Sn-W occurrences, the Mawchi mine is a world class Sn-W deposit with estimated ore reserves of
118 350,000 tons (Htay et al., 1997). Mawchi is situated 219 km southeast of Naypyitaw and was the
119 world's largest granite-hosted tin-tungsten vein system before World War II. During the period of
120 1930-1940 the company produced 2000 to 6000 tonnes of ore annually, amounting to 60% of the
121 total production of Myanmar. Approximately 25,000 tonnes of Sn-W ore were produced from
122 1980-2010 (unpublished Mawchi mine data). Although there is some literature describing the
123 geology of Mawchi mine and surrounding area (Dunn, 1938; Hobson, 1941; Zaw and Thet, 1983;

Myint et al., 2017a), no new data have been published relevant to the ore deposit geology of Mawchi mine in recent years. Here we present and discuss new data associated with the mineralogy, fluid inclusion microthermometry, stable isotope and, $^{40}Ar/^{39}Ar$ and Re-Os geochronology of the Mawchi deposit to constrain the ore genesis and timing of the Sn-W mineralization and implications for Sn-W deposit exploration in the WGP.

2. Geological background

2.1 *Regional geologic setting*

As shown in (Fig. 1a) the MMB lies immediately west of the mineralized WGP granites. The MMB also hosts S- type granites but these lack tin mineralization, perhaps because of either a deeper erosion level or source rock different to that which produced the partial melts which resulted in the mineralized granites. The WGP contains Cretaceous to Tertiary granitoid rocks of metaluminous to peraluminous, high K calc-alkaline composition (Cobbing et al., 1992; Mitchell et al., 2012; Myint et al., 2017a&b). Miocene granitic dyke rocks cut the older granitic rocks in some places. The Sn-W mineralization is predominantly associated with granites, granite pegmatites and aplite dykes from the WGP which intruded Carboniferous to Early Permian metasedimentary and sedimentary sequences of the Slate Belt (SB; Bender 1983; Mitchell et al., 2004; Myint et al., 2013; Myint et al., 2017a). The SB comprises the sediments and low grade metasediments of Lebyin, Mawchi and Mergui Groups in Myanmar and Kaeng Krachan Group in

143 Thailand.

144 The MMB is a high-grade metamorphic sequence of gneiss, schists and marbles. In the
145 northern part of the belt around Mogok, ruby-bearing phlogopite–diopside–graphite–spinel–
146 bearing marble or calc-silicate and sapphire-bearing post-deformation pegmatitic nepheline
147 syenites are found (Iyer, 1953; Mitchell et al., 2007). The marbles are probably metamorphosed
148 from either the Precambrian (Chhibber, 1934) or Precambrian to Jurassic rocks of the Shan Plateau
149 (Searle and Haq, 1964). Some units of meta-igneous rocks and marbles at and west of Mogok have
150 been correlated with the Silurian and Ordovician units of the Shan Plateau (Thein et al., 1988).
151 Around the Mandalay-Kyaukse-Tharzi areas, the MMB is mostly composed of marbles and calc-
152 silicate rocks with minor schists and gneiss. Some outcrops of low-grade marble contain relict
153 Ordovician to Permian fossils. The fossiliferous rocks and probably the marble and calc-silicates
154 in this segment of the MMB are part of the Paleozoic to Triassic Plateau sequence. Garnet and
155 sillimanite schists with augen gneisses and minor marble continue southwards to the Andaman Sea
156 coast occupying a parallel belt to the WGP and SB.

157 The Mawchi Sn-W deposit is located in the eastern part of Myanmar. The regional
158 geology is comprised by the NNW-SSE trending juxtaposition of the Mogok Metamorphic Belt
159 (MMB; Searle and Haq, 1964; Mitchell et al., 2007) and metasedimentary and sedimentary rocks
160 of the Mawchi Group (a part of SB) amalgamated with a succession comprising Paleozoic to
161 Triassic shallow marine carbonates and sediments with Jurassic and Cretaceous continental

sediments (Fig. 1b).

Permian Plateau Limestone occurs as NNW-SSE trending intermittent limestone caps on the metasediments and granite striking parallel to shear splays. The prominent rocks of the Mawchi Group are hornfels, mudstones, fine-grained sandstone and metagreywacke. Grayish and reddish colored fine-grained sandstones, argillite and phyllite are common, and grayish and reddish mudstones and claystones occur interbedded between sandstone and argillite in some localities.

2.2 *Geology of Mawchi Sn-W district*

The geology of the area is characterized by the metamorphic rocks of MMB, metasedimentary rocks of Carboniferous to Early Permian Mawchi Group (Myint et al. 2017a), Permian Plateau Limestone and intrusive bodies of biotite granite and tourmaline granite of WGP (Hobson, 1941; Myint et al., 2017a) (Fig. 2a). Metamorphic rocks of the MMB, containing gneisses, granite gneisses and schists, are found in the western part of Mawchi area and their contact with the Mawchi Group appears to be defined by a fault. The Mawchi Group shows extreme lithological variations, including; mudstone, shale, fine-grained siltstone and sandstone, slate, quartzite and metagreywacke. Elongate and small granite bodies of the WGP are dispersed and intrude the metasedimentary rocks and Permian Plateau Limestone along NNW-SSE fracture systems. Most

of these granite bodies are coarse-grained porphyritic biotite granites with accessory epidote and apatite (Hobson, 1941).

In the Mawchi Mine area, a granite pluton is composed of medium- to coarse-grained biotite granite, grading into fine- to coarse-grained tourmaline granite towards the mineralized zone. Pervasive tourmalinization is superimposed on the biotite granite. The biotite granite is mainly composed of quartz, feldspar, biotite with trace amount of tourmaline and contains high silica content (74 - 86 wt. %) with A/CNK [molecular Al_2O_3 / CaO + Na_2O + K_2O)] >1. It possesses minor hydrothermal alteration characterized by a trace presence of hydrothermal tourmaline. The tourmaline granite consists of quartz, feldspar, muscovite and tourmaline (Myint et al., 2017a). Biotite is rare in the tourmaline granite. Hydrothermal muscovite-sericite clusters or aggregates are commonly associated with and occasionally replace tourmaline. Spider diagrams for the Mawchi granites show with pronounced negative Ba, Sr, Nb and Ti anomalies with positive Rb, Pb, U anomalies and the granites have low Nb/Ta and Zr/Hf values. These granites were derived from a magma generated by the melting of crustal rocks and extensive magmatic differentiation. Trace element geochemistry and the low εNd (T) values reveal that distinct crustal sources have been involved in emplacement of the peraluminous granitic rocks and their Sn-W enrichment (Myint et al., 2017a). The LA-ICP-MS U-Pb zircon ages of the biotite and tourmaline granites are 42.72 ± 0.94 Ma (n = 12; MSWD = 2) and 43.71 ± 0.39 Ma (n = 12; MSWD = 1.02), respectively (Myint et al., 2017a). Petrographic, geochemical and geochronological studies

199 indicate that the tourmaline granite of Mawchi mine area is a hydrothermally altered biotite granite
200 (Myint et al., 2017a).

201 Several satellite Sn-W prospects surround the Mawchi deposit, comprising;
202 Htawmawkhee, Ketaunggalay, Hteelakhee and Mosakhee. The Htawmawkhee prospect is
203 composed of parallel and inclined small quartz veins that strike NW-SE. These 2 to 14 cm thick
204 veins are hosted by argillite and contain cassiterite, wolframite and tourmaline. Nearly N-S
205 trending sheeted veins are also observed. In the Ketaunggalay prospect, wolframite-bearing quartz
206 and pegmatite veins are hosted by metasandstone of the Mergui Group and strike in a nearly N-S
207 direction. Hteelakhee is 12 km south of the Mawchi mine and is characterized by cassiterite and
208 wolframite bearing quartz veins and sheeted veins hosted by the argillite and sandstone. The
209 Mosakhee prospect is situated near the village of Mosakhee where wolframite and stannite are
210 associated with some sulfides such as galena and sphalerite (Myint, 2015). The quartz veins trend
211 N-S and are hosted by the metasediments.

212

213 **3. Mawchi Sn-W mineralization**

214 The Mawchi ore body is classified into three types according to vein geometry and mineral
215 assemblage. The principal mineralization is represented by cassiterite-wolframite bearing quartz
216 veins that are hosted by the tourmaline granite and metasedimentary rocks (Fig. 2b&c). These

veins are generally confined to a N-S trending fracture system (Fig. 3a), which upwardly taper forming a minor stockwork style vein network (Fig. 3b). In the vein system close to the limestone, scheelite-danalite assemblage form a skarn assemblage. Danalite occurs as bands parallel to the vein wall (Fig. 3c) or as irregular patches in the vein. Post-mineralized veins are horizontal and gently inclined, cutting through mostly metasedimentary rocks. These veins are, generally, quartz-tourmaline veins and are barren of ore minerals and are common in the uppermost part of the ore body (Fig. 3d).

Cassiterite and wolframite occur in the marginal zone (Fig. 3e) as well as in the central zone of the veins, whereas sulfide minerals occur only in the central zone, suggesting that oxide ore minerals crystallized early and sulfide minerals late in the paragenetic sequence. Fractures are occasionally observed to host an early formed mineral assemblage of tourmaline – cassiterite ± pyrite (Fig. 3f). Massive bands and pockets of cassiterite ± tourmaline ± muscovite ± pyrite are also common at the vein margins (Fig. 3g).

The common gangue minerals in the Mawchi vein system are tourmaline, micas (muscovite, sericite, gilbertite, and lepidolite), danalite, fluorite, chlorite, clay minerals (kaolinite, illite), calcite and beryl. Tourmaline, the most common gangue mineral, is dispersed widely, not only in the veins, but also in the host rocks. Tourmaline also represents the dominant alteration associated with Sn-W mineralization, with its deposition preceding that of wolframite and other sulfides in some cases. Other common alteration assemblages are albitization, sericitization,

236 silicification and kaolinization. Albitization occurs in the highly tourmalinized granite (Myint et
237 al., 2017) whereas sericitization is characterized by the mica selvages along the contact of host
238 rock and quartz veins. The sericitization postdates the tourmalinization as can be seen clearly in
239 the tourmaline granite (Fig. 3h).

240 Assay data corresponding to the veins from various levels are tabulated in Table 1 and
241 indicate a downward decrease of Sn and WO_3 content. The Sn:WO_3 varies among different veins
242 ranging mostly between 1: 0.7 and 1: 0.5.

243

244 **4. Methodology**

245 4.1 *Mineralogical and fluid inclusion study*

246

247 The mineralogical study utilized transmitted and reflected light microscopy, and x-ray
248 diffractometry (XRD), Scanning Electron Microscopy (SEM), and Electro Probe Micro Analysis
249 (EPMA). The mineral identification by the XRD method was performed using a Rigaku Ultima
250 IV X-ray Diffractometer at the Economic Geology Laboratory, Kyushu University. Elemental
251 analyses were performed using a Shimadzu Superscan SSX-550, equipped with an energy-
252 dispersive x-ray analyzer (SEM-EDX) at the Advanced Research Center and a JEOL JXA8530F
253 field emission EPMA at the Department of Environmental Changes, Kyushu University. The fluid

254 inclusion analysis were performed by measuring the final ice melting point (salinity calculations)
255 and heating the fluid inclusion samples (homogenization temperature) using a calibrated Linkam-
256 THMS600 heating-freezing stage.
257
258 4.2 *Ar-Ar methods*
259
260 Magmatic biotites from the biotite granite of the Mawchi area were separated with the
261 objective of determining the magmatic cooling age. Hydrothermal muscovites from the tourmaline
262 granite exposed near the mine site and a quartz vein from an underground working in the deposit
263 were selected to determine the timing of alteration that is later than thr tourmalinization which is
264 spatially and genetically associated with the Sn-W ore deposition.
265 Mica samples were irradiated together with the TCR sanidine standard (batch 2; 28.34Ma
266 recalculated by Renne et al., 1998) at the NRG-Pattern HFR Rodeo facility in the Netherlands, and
267 later analyzed at Lund University, Sweden using a Micromass 5400 Mass Spectrometer with a
268 Faraday and an electron multiplier. The mass spectrometer is equipped with a metal extraction
269 line, containing two SAES C50-ST101 Zr-Al getters and a cold finger cooled to app. -155˚C by a
270 Polycold P100 cryogenic refrigeration unit. One or two grains of mica were loaded into a copper
271 planchette consisting of a number of 3 mm holes. Samples were step-heated using a defocused
272 50W CO_2 laser rastered over the samples to provide even heating of all grains. Sample clean up

273 times were 5 min (using two hot Zr-Al getters and a cold finger). The laser was rastered over the
274 samples to provide even heating of all grains. The analytical process is automated and runs on a
275 Macintosh OS 10.2 platform with software modified specifically for the laboratory at the
276 University of Lund. Time zero regressions were fitted to data collected from 10 scans over the
277 mass range of 36 to 40. Peak heights and backgrounds were corrected for the mass discrimination,
278 isotopic decay and interfering nucleogenic Ca-, K-, and Cl-derived isotopes. Isotopic production
279 values for the cadmium lined position in the Petten reactor are $^{36}Ar/^{37}Ar(Ca)$ = 0.000270,
280 $^{39}Ar/^{37}Ar(Ca)$ = 0.000699, and $^{40}Ar/^{39}Ar(K)$ = 0.00183.

281 Blanks were measured before each sample and after every three-sample step. Blank values
282 were subtracted from the sample signal for all incremental steps. Age plateaus were determined
283 following the criteria of Dalrymple and Lanphere (1971), specifying the presence of at least three
284 contiguous incremental heating steps with statistically indistinguishable ages and constituting
285 more than 50 % of the total ^{39}Ar released during the experiment. Plateau ages are quoted with
286 uncertainties at the 2σ level (Hermansson et al., 2008). The Taylor Creek Rhyolite (TCR) sanidine
287 standard (28.34 ± 0.16 Ma; Renne et al., 1998) was used as flux monitor. J-values were calibrated
288 with a precision of 0.25 %. The uncertainties in the *J*-values have been propagated into the
289 uncertainties in the plateau ages. However, the uncertainties in the decay constant and in the
290 standards are not propagated.

291

292 4.3 *Re-Os methods*

293

294 The molybdenite in the Mawchi deposit is fine-grained (0.2 – 1 mm) and rare. The
295 molybdenite is associated with cassiterite-wolframite-sulfides bearing quartz-tourmaline vein, and
296 possesses mica and tourmaline selvages. Molybdenite from one sample was physically (crushed,
297 magnetic and heavy liquid separation, and hand-picked) isolated from a quartz vein to yield a
298 mineral separate of several tens of milligrams.

299 Rhenium-osmium (Re-Os) analysis was conducted using isotope-dilution negative
300 ionization mass spectrometry at Durham University (Selby and Creaser, 2001). The molybdenite
301 sample, together with a known amount of tracer solution (^{185}Re + normal Os) was digested in a
302 carius tube with 3 mL HCl (11 N) and 6 mL (15 N HNO_3) at 220˚C for 24 hours. Osmium from
303 the acid solution was isolated via solvent extraction ($CHCl_3$), and purified by using micro-
304 distillation. The Re from the Os extracted solution was extracted via NaOH-Acetone extraction
305 and purified by anion chromatography (Cumming et al., 2012). The isolated Re and Os fractions
306 were loaded onto Ni and Pt wire filaments, respectively, with the isotope compositions determined
307 via Faraday cups of a Thermo Scientific TRITON mass spectrometer. The Re-Os data are blank
308 corrected using values of 2 ± 0.03 ppt for Re, 0.11 ± 0.04 ppt for Os, with an ^{187}Os/^{188}Os of 0.25
309 ± 0.02. The Model Re-Os age is calculated using the equation ln (^{187}Os/^{187}Re + 1)/**λ**, using the
310 decay constant (**λ**) of 1.666e^{-11}a^{-1} (Smoliar et al., 1996). Uncertainties include all sources of

311 analytical uncertainty (Re and Os mass spectrometer measurements, blank abundances and
312 isotopic compositions, spike calibrations and reproducibility of standard Re and Os isotopic
313 values), both with and without the uncertainty in the decay constant (0.35%; Smoliar et al., 1996;
314 Selby et al., 2007). All uncertainties are presented at the 2σ absolute level.
315
316 4.4 *Stable isotopic analysis*
317 Stable isotope compositions were analyzed at the Scottish Universities Environmental
318 Research Centre (SUERC), UK. For O-isotopic analyses, mineral separates (cassiterite,
319 wolframite, tourmaline, quartz and scheelite) were analyzed by the laser fluorination procedure,
320 involving total sample reaction with excess ClF_3 using a CO_2 laser as a heat source (in excess of
321 1500°C). All combustions resulted in 100% release of O_2 from the mineral lattice. Liberated O_2
322 was then converted to CO_2 by reaction with hot graphite, then analyzed on-line using a VG SIRA
323 10 spectrometer. Reproducibility is ~ ± 0.3 ‰. Results are reported in standard notation ($\delta^{18}O$) as
324 per mil (‰) deviations from the Standard Mean Ocean Water (V-SMOW) standard.
325 Pyrite, arsenopyrite, chalcopyrite, sphalerite, galena and Pb-Bi sulfides were selected for
326 sulfur isotope analyses. Pyrite-I and Pb-Bi sulfides were prepared for conventional isotopic
327 analysis by standard heavy liquid (sodium polytungstate) and hand picking techniques. One gram
328 of sample was collected from each although around 5 to 10 mg were utilized for isotopic analysis.
329 Minor contamination by non S-bearing phases was tolerated, and has no isotopic effect on the final

data. Sulfides were analyzed by standard techniques (Robinson and Kusakabe, 1975) in which SO_2 gas was liberated by combusting the sulfides with excess Cu_2O at 1075°C, *in-vacuo*.

Other sulfides such as pyrite-II, arsenopyrite, chalcopyrite, galena and sphalerite were examined by *in-situ* laser combustion from standard polished blocks. The blocks were inserted into a sample chamber, which was evacuated and subsequently filled with an excess of oxygen gas (Fallick et al., 1992). The spatial resolution is determined by the minimum volume of SO_2 gas required for analysis (0.05–0.10 µmol), with minimum spot sizes of approximately <100 µm. Samples were rastered under the laser beam to combust individual zones extending around 500 by 100 µm. The laser beam was a SPECTRON LASERS 902Q CW Nd:YAG laser (1 W power), operating in TEM_{00} mode. The SO_2 gas produced by each laser combustion was purified in a miniaturized glass extraction line, using a CO_2/acetone slush trap to remove water and a standard *n*-pentane trap to separate SO_2 and trace CO_2 (Kelley and Fallick, 1990). Determination of the sulfur isotope composition of the purified SO_2 gas was carried out on-line by a VG SIRA II gas mass spectrometer.

The international standards employed to calibrate the reference gas were NBS-123 and IAEA-S-3, and SUERC standard CP-1 which gave $\delta^{34}S$ values of +17.1‰, -31.5‰ and -4.6‰ respectively, with 1σ reproducibility around ±0.2 ‰ in this study. Data are reported in $\delta^{34}S$ notation as per mil (‰) variations from the Vienna Canyon Diablo Troilite (V-CDT) standard. The laser extraction method results in a sulfur isotope fractionation between the host mineral and the SO_2

gas produced via combustion, which is mineral-specific (Kelley and Fallick, 1990). Experimentally determined fractionation factors are currently available in the SUERC system to apply correction to several sulfide/sulfosalt minerals, for example, pyrite (+0.8 ‰) and galena (+2.4 ‰). Further discussion of the laser-induced fractionation is given in Wagner et al. (2002).

For H isotope analysis of fluid inclusion water, pure mineral samples of cassiterite, wolframite and quartz (around 1 g) with one dominant fluid inclusion population, were heated to 100°C overnight under high vacuum to release labile volatiles and loaded into outgassed Pt crucibles. Samples were gradually heated by radiofrequency induction in an evacuated quartz tube to temperatures in excess of 700°C. For H isotope analysis of tourmaline, pure samples of ~ 800 mg were heated to 150°C overnight under high vacuum to release labile volatiles after loading into outgassed Pt crucibles. Samples were then gradually heated by radiofrequency induction in an evacuated quartz tube to temperatures in excess of 1200°C. The released water was reduced to H_2 in a chromium furnace at 800°C (Donnelly et al., 2001), with the evolved gas measured quantitatively in an Hg manometer, then collected using a Toepler pump. The gas was subsequently analyzed on a VG 602D mass spectrometer with a manual Hg, high gas compression inlet system. Replicate analyses of international water standards (V-SMOW and GISP), and an internal standard (Lt Std) gave a reproducibility of ± 2 ‰. Replicate analyses of the international mineral standard NBS-30 (biotite) also gave reproducibility around ± 2 ‰. A more conservative error for fluid inclusion samples would be around ± 5 ‰.

5. Mineralogy and vein paragenesis

The paragenetic sequence of ore deposition in the Mawchi vein system is presented in Fig. 4 and has been divided into three stages.

5.1 *Tourmaline-cassiterite stage*

The onset of ore deposition was initiated by pervasive tourmalinization with tin mineralization. Early-formed tourmaline in the tourmaline granite is likely the precursor of quartz vein deposition and successive deposition of late tourmaline and cassiterite took place not only along the small fractures and vein boundary as masses and patches, but also in the highly altered tourmalinized granitic rocks. In such case, wolframite is rarely found with tourmaline and cassiterite, and, these early-formed minerals coexist with first generation of pyrite (pyrite-I) in some places. Cassiterite is the major ore mineral in this stage and has been identified as idiomorphic crystals as well as a massive band with tourmaline, muscovite and pyrite-I at the vein margin. Sometimes, fine tourmaline segregations with the cassiterite can be found as dark-colored patches in the vein. Pyrite-I crystals are, generally idiomorphic or sub-idiomorphic, up to 0.3 mm long and usually dispersed in both the granite body and veins showing it formed before wolframite. The late phase of this stage overlapped with the main ore stage and continued until the end of oxide ore deposition.

5.2 *Main ore stage*

387 The second stage of ore deposition (main ore stage) in the Mawchi vein system appears to
388 have begun with the precipitation of major oxide ore minerals such as cassiterite, wolframite and
389 scheelite with subordinate amount of such sulfide minerals as molybdenite, arsenopyrite and
390 second generation pyrite (pyrite-II) (Fig. 5a). Minute molybdenite flakes commonly occur in the
391 deep level vein system and are affected by kink banding adjacent to the undeformed mineral grains
392 such as pyrite-II and chalcopyrite, and pyrite-II penetrates the cleavage plane of molybdenite (Fig.
393 5b). Molybdenite occurs as isolated flakes in quartz or in tourmaline or at the border of wolfram
394 and quartz (Dunn, 1938). Cassiterite has been identified as idiomorphic crystals as well as forming
395 a mixed matrix with wolframite, arsenopyrite and pyrite in the vein. Color zoning is common (Fig.
396 5c). Wolframite is the principal tungsten mineral of the Mawchi mine and it can be found either as
397 large dispersed crystals or intergrown with cassiterite and/or with sulfide minerals. Marginal
398 replacement by early-formed sulfide minerals (Fig. 5d) and scheelite replacement are common
399 (Fig. 5e) in wolframite. Although ferberitic in some veins, wolframites from Mawchi veins are
400 compositionally mostly hubneritic to wolframitic in composition. The first generation wolframite
401 is generally wolframitic and intergrown with cassiterite, with the second generation wolframite,
402 which contemporaneously appears with pyrite-II, is mostly of hubneritic composition.
403 Two distinct generations of pyrite with several modes of formation are identified. Pyrite-I,
404 occurring in considerable amounts and as tiny cubes, is the earliest sulfide mineral followed by
405 pyrite-II and arsenopyrite. Pyrite-II occurs very widely and shows a cataclastic texture in some

places. Pyrite-II formed simultaneously with or somewhat later than arsenopyrite. In the vein system, pyrite-I cubes are surrounded by the fractured pyrite-II and other later-formed sulfides, such as arsenopyrite (Fig. 5f). Clusters of minute acicular pyrite are also observed in the lower part of veins as void-filling minerals among the other ore and gangue minerals. Scheelite forms mainly as a secondary mineral replacing wolframite and partly as milky white to yellowish white crystals in veins (Fig. 5g) close to the contact of limestone and granite. Scheelite is associated with danalite, wolframite, cassiterite and tourmaline, suggesting a skarn forming event. Some scheelite crystals contain tourmaline (Fig. 5h) and cassiterite as inclusions. Interstitial filling of pyrite-II between the grains of cassiterite and wolframite is common (Fig. 6a). Arsenopyrite, one of the most common and abundant of vein sulfides, frequently occurs as anhedral aggregates and is sometimes intergrown with pyrite-II. Most arsenopyrite formed early in the vein sequence, evidently overlapping wolframite and some early generation pyrite-II.

Tourmaline and muscovite-sericite are still common in the main ore stage and danalite, chlorite, early fluorite are other common gangue minerals. After the main ore and sulfide stages, tourmaline continued to deposit together with quartz. Fluorite, another common gangue mineral, is of two distinct types, which differ in color and mode of occurrence. The first fluorite species is generally bluish to purplish or greenish in color spatially associated with wolframite, cassiterite (Fig. 6b), tourmaline, chlorite and muscovite-sericite. Another species of fluorite is mostly greenish color enriched in yttrium and forms yttrofluorite in some places. It is the product of

425 hydrothermal activity, which was either early or contemporaneous with the deposition of Nb-Ta-
426 REE minerals of the sulfide stage.

427 5.3 *Sulfide stage*

428 The third stage (Sulfide stage) is defined by the successive deposition of sulfide minerals
429 such as chalcopyrite, sphalerite, galena and Pb-Bi sulfides with minor formation of fergusonite,
430 wolframo-ixiolite and other Nb-Ta minerals. Tiny and dispersed fergusonite, wolframoixiolite
431 (Fig. 6c), Nb-bearing rutile and other Nb oxide minerals are common in the lower levels of the
432 Mawchi vein system where the mineralization is hosted by granite. The Nb-Ta minerals are
433 probably the result of exsolution and replacement of scheelite and hubneritic wolframite (Myint et
434 al. in review). Sphalerite occurs not only as a replacement mineral in the interstices and grain
435 boundaries of arsenopyrite and pyrite crystals, but also as inclusions in galena. It usually contains
436 2.4 – 11.6 wt. % Fe, and encloses blebs and tolls of chalcopyrite and stannite, forming as an
437 exsolution pattern (Fig. 6d). Therefore, sphalerite is contemporaneous with chalcopyrite, but
438 younger than arsenopyrite and pyrite, and older than galena. Chalcopyrite occurs not only as tiny
439 veinlets and replacements (type-I) in arsenopyrite, pyrite and other early vein minerals (Fig. 6e),
440 but also as anhedral grains (type-II) (Fig. 6f). Galena is a late sulfide mineral following sphalerite,
441 replacing the former sulfides and enclosing them as inclusions. Galena can be found as marginal
442 replacement along the borders of chalcopyrite and sphalerite (Fig. 6g), along the fractures of pyrite
443 grains, and as scattered mineral grains in the quartz. The galena and sphalerite are sometimes

444 veined by cerussite.

445 The later phase of the sulfide stage is marked by the deposition of bismuth-bearing galena
446 and other bismuth-lead sulfides. These are widespread in the veins and replace early-formed
447 sulfides of pyrite, chalcopyrite and sphalerite (Fig. 6h). The bismuth-bearing galena contains 0.23
448 - 1.37 wt. % Bi, whereas Bi-Pb sulfides (including cosalite) contain 0.2 - 1.76 wt. % Ag. Pyrrhotite
449 is found as very rare accessory and, hematite, covellite, chalcocite and cerussite occur as supergene
450 minerals.

451

452 **6. Results**

453 6.1 *Ar-Ar and Re-Os dating*

454 Mica Ar-Ar data is presented in Table 4 and, plateau age and isochron diagrams are shown
455 in Fig. 7. Magmatic biotite from the biotite granite at Mawchi yields a well-defined plateau age of
456 41.50 ± 0.16 Ma (MSWD = 2.5), with an inverse isochron date of 42.4 ± 0.3 Ma (MSWD = 1.7).
457 The hydrothermal muscovites dated from the tourmaline granite and a quartz vein give plateau
458 ages of 40.14 ± 0.14 Ma (MSWD = 1.48) and 40.80 ± 0.12 Ma (MSWD = 0.47) respectively. The
459 plateau ages are consistent with the inverse isochron dates of 40.20 ± 0.3 Ma (MSWD = 1.7) and
460 40.73 ± 0.17 Ma (MSWD = 1.5), respectively. The Re-Os abundances and model age of quartz
461 vein-hosted molybdenite are given in Table 5. The concentrations of Re and ^{187}Os of the Mawchi
462 molybdenite are 1.36 ppm and 0.61 ppb, respectively. The Re-Os data yield a Re-Os model age of

463 42.43 ± 1.21 [42.43 ± 1.22 including the uncertainty in the decay constant] Ma.

464

465 6.2 *Fluid inclusions microthermometry*

466 Liquid-rich two-phase (liquid and vapor) primary fluid inclusions are dominant in massive
467 cassiterite and in cassiterite, scheelite and quartz from the main ore stage and, quartz and fluorite
468 from sulfide stage. Fluid inclusions vary from being circular through tubular to irregular in shape,
469 and are between 7 and 25µm in size. The homogenization temperatures (Th) in primary fluid
470 inclusions of massive cassiterite from cassiterite-tourmaline stage range from 311˚ to 343˚C (Fig.
471 8), with final ice melting temperatures of -2.7˚ to -7.9˚C suggesting moderate salinity (4.5 to 11
472 wt. % NaCl equiv) (Fig. 9). Primary inclusions in vein cassiterite, formed during the main ore
473 stage with tourmaline, homogenized between 312˚ and 340˚C and exhibit ice melting temperatures
474 of -2.5˚ to -5.6˚C, corresponding to salinities of 4.7- 11.9 wt. % NaCl equiv. Fluid inclusions in
475 scheelite from the quartz veins record moderate homogenization temperatures (261˚ -313˚C) and
476 final ice melting temperatures that indicates moderate salinity (6.8 – 15.7 wt % NaCl equiv).

477 Based on salinity, fluid inclusions of fluorite from sulfide stage can be divided into two
478 groups: low salinity (2.5 – 5 wt. % NaCl equiv) inclusions with low Th (174˚ - 185˚C) and,
479 moderate salinity (10– 13 wt. % NaCl equiv) inclusions with low Th (175˚ - 220˚C). Quartz
480 samples from were also studied, yielding Th of 180˚ to 290˚C, similar to temperatures reported by
481 Zaw and Thet (1983), and low salinity (3.5 – 7.7 wt. % NaCl equiv).

482

483 6.3 *Stable isotopic systematics*

484 6.3.1 *Sulfur isotopes*

485 A total of 45 samples of sulfide minerals from all stages of mineral paragenesis were
486 analyzed to ascertain the source of sulfur in the mineralization of the Mawchi deposit.

487 The $\delta^{34}S$ data are listed in Table 2 and plotted in Fig. 10.

488 Pyrite-I from the tourmaline granite and vein samples, which are the representatives of the
489 tourmaline-cassiterite stage, yield $\delta^{34}S$ values of +5 ‰ and +5.6 ‰. Pyrite-II and arsenopyrite
490 from the main ore stage gave $\delta^{34}S$ values of 3.8 to 6.2 ‰ and 2.5 to 3.6 ‰, respectively.

491 Chalcopyrite, sphalerite and galena from the sulfide stage reveal a broader range in $\delta^{34}S$
492 values, with type-II chalcopyrite possessing $\delta^{34}S$ values from 0.9 - 1.1 ‰, whereas type-I yields
493 two populations of $\delta^{34}S$ values, 4.5 - 6.2 ‰ and 9.4 - 10.6 ‰. The $\delta^{34}S$ values of sphalerite range
494 between -3.2 and 3.2 ‰. Galena defines a narrow range in $\delta^{34}S$ values of -1.3 to 1.8 ‰.

495 The final stage of mineralization, bismuth-bearing galena and Pb-Bi sulfides yield $\delta^{34}S$
496 values of 0.7 - 2.7 ‰, which are quite similar to those of galena. Overall, the entire sulfide set
497 from Mawchi defines a narrow $\delta^{34}S$ range around a mean of 2.9 ± 2.9‰ (1σ; N=45).

498

499 6.3.2 *Oxygen and hydrogen isotopes*

500 Oxygen and hydrogen isotopes were analyzed to identify the source of ore fluid. The

501 $\delta^{18}O_{mineral}$, calculated $\delta^{18}O_{H2O}$ and hydrogen isotope data of vein minerals are listed in Table 3. The

502 calculated $\delta^{18}O_{H2O}$ data of vein minerals are presented in Fig. 11.

503 The mean homogenization temperature of fluid inclusions in vein hosted main ore stage

504 cassiterite, 325˚C, is used to calculate the $\delta^{18}O_{H2O}$ values of cassiterite with coexisting tourmaline.

505 The $\delta^{18}O_{H2O}$ values calculated for scheelite and quartz from main ore stage are based on their

506 respective mean fluid inclusion homogenization temperatures of 290˚ and 280˚C. From the

507 paragenetic sequence, the temperature of formation of wolframite ranges between 325˚ and 290˚C.

508 Thus 310˚C was fixed to calculate the best estimate of $\delta^{18}O_{H2O}$ values of wolframite. The $\delta^{18}O_{H2O}$

509 values for quartz from main ore stage and sulfide stage are based on their respective mean fluid

510 inclusion homogenization temperatures of 280˚ and 260˚C, respectively.

511 The $\delta^{18}O$ values of cassiterite from the Mawchi veins show a narrow range between 4.6

512 and 5.7 ‰, with the exception of samples from the stockwork zone (nekhee-1 &-2) that possesses

513 heavier $\delta^{18}O_{H2O}$ values of 8.3 and 8.4 ‰. The calculated $\delta^{18}O_{H2O}$ at 325˚C is 7.3 to 11.1 ‰. The

514 $\delta^{18}O$ values of tourmalines are distinctly homogeneous (10.4 - 10.8 ‰) and the $\delta^{18}O_{H2O}$ values

515 range from 7.8 to 8.2 ‰ at an estimated temperature of 325˚C. Wolframite has relatively lighter

516 $\delta^{18}O$ values compared to cassiterite and tourmaline ranging from 2 to 4.3 ‰, with calculated

517 $\delta^{18}O_{H2O}$ values of 3.9 to 6.2 ‰. Scheelite has $\delta^{18}O$ of 0.6 to 2.7 ‰, with calculated $\delta^{18}O_{H2O}$ values

518 of 2.1 to 4.2 ‰. The $\delta^{18}O$ values of quartz samples from various veins range from 11.5 to 13.4 ‰

519 and their calculated $\delta^{18}O_{H2O}$ values range from 3 to 4.9 ‰.

520 Inclusion fluids were extracted to determine the δD value of fluids associated with the
521 formation of cassiterite, wolframite and quartz in the Mawchi veins. The hydrogen isotope
522 compositions of tourmaline were also analyzed, yielding $\delta D_{tourmaline}$ values of -112 to -99 ‰. Four
523 cassiterite samples from the main ore stage and one from the tourmaline-cassiterite stage were
524 analyzed and their fluid inclusions gave δD_{H_2O} values from -86 to -51 ‰. Three wolframite
525 samples from granite-hosted veins and two samples from metasediment-hosted veins gave δD_{H_2O}
526 values of -87 to -61 ‰ and -121 to -118 ‰, respectively. Most of the quartz samples have dominant
527 secondary fluid inclusions and, hence, two granite-hosted veins representing the main ore stage
528 that have mostly primary fluid inclusions were selected for a hydrogen isotope study. They yield
529 δD_{H_2O} values of -85.3 and -78.4 ‰.
530
531 **7. Discussion**
532 7.1 *Timing of magmatic-hydrothermal activity*
533 The zircon LA-ICP-MS U-Pb ages of 42.72 ± 0.94 Ma and 43.71 ± 0.39 Ma have been
534 interpreted as the crystallization age of zircons and the emplacement age of the Mawchi pluton
535 (Myint et al., 2017). The magmatic biotite Ar-Ar plateau age of 41.50 ± 0.16 Ma is in agreement
536 with the zircon U-Pb ages, however the nominally younger age of the Ar-Ar biotite age suggest
537 that this date represents the timing of igneous cooling below the blocking temperature (~350˚C)
538 for Ar in biotite. The hydrothermal muscovite in the tourmaline granite (40.14 ± 0.14 Ma) and in

539 the vein selvage (40.80 ± 0.12 Ma) yield similar Ar-Ar dates, indicating a broadly
540 contemporaneous formation. The Ar-Ar ages agree with the paragenetic relationships. The biotite
541 $^{40}Ar/^{39}Ar$ plateau age represents cooling during the magmatic event, with the muscovite Ar-Ar
542 plateau ages corresponding to the late stage hydrothermal alteration that formed after
543 tourmalinization (i.e. tourmaline-cassiterite and main ore stages).

544 The molybdenite Re-Os age of 42.43 ± 1.21 Ma also reveals the timing of mineralization
545 and, it agrees with the U-Pb zircon age and biotite Ar-Ar date suggesting that ore deposition was
546 essentially coeval with magmatic crystallization and fluid exsolution. The Re-Os age represents
547 the main ore stage mineralization and muscovite Ar-Ar age expresses the late stage hydrothermal
548 alteration.

549

550 7.2 *Source of sulfur*

551 The $\delta^{34}S$ values of pyrite and arsenopyrite range from 2.9 to 6.2 ‰ and from 2.5 to 5.2
552 ‰ respectively, indicating a relatively homogeneous source, likely dominated by magmatic sulfur
553 in tourmaline-cassiterite and main ore stages. In the later, sulfide stage, type-II chalcopyrite
554 possesses $\delta^{34}S$ values between 4.5 and 10.6 ‰ - suggesting a more reduced state than the main ore
555 stage – compared to type-I chalcopyrite grains that exhibit $\delta^{34}S$ values of 0.9 to 1.1‰. Sulfur
556 isotope data for sphalerite shows evidence for a lighter source of S (-3.2 to 3.2 ‰), with galena
557 and Pb-Bi sulfides yielding a narrower range in $\delta^{34}S$ values (-1.3 to 2.7‰). The similarity of $\delta^{34}S$

values, close to 0 ‰ in galena and Pb-Bi sulfides, may indicate that Pb and Bi were transported by a common fluid of purely magmatic origin. Apart from the heavier sulfur in type- I chalcopyrite, the principal feature of the sulfur isotope data is the systematic decrease from around 5-5.4 ‰ to 0-2 ‰ in $\delta^{34}S$ with paragenetic sequence (Fig. 10). The $\delta^{34}S$ of pyrite-I (5 - 5.4 ‰) in tourmaline-cassiterite stage also coincides with that for crustal-derived granite (Kohut and Recio, 2002; Cao et al., 2016) suggesting that the sulfur in the tourmaline-cassiterite and main ore stages is mainly crustally-derived. The crustal or heavier sulfur isotopic components appear to become progressively lighter during the progressive deposition of the sulfides in the sulfide mineral paragenesis.

Assuming ranges of depositional temperature of 340˚ to 260˚C for main ore stage, possible $\delta^{34}S_{H_2S}$ values of pyrite-II are 2.3 to 5.0 ‰ (using the data of Omoto and Rye, 1979), and with the mean of all sulfide $\delta^{34}S$ being 2.9 ± 2.9 ‰, suggesting that the overall system is dominated by magmatic sulfur (Omoto and Rye, 1979; Wagner et al., 2005; Wagner et al., 2009). Since sulfide stage chalcopyrite occurs after the main ore stage deposition, a temperature range of 260˚ to 230˚ C is assumed for type-I and –II chalcopyrite. According to Li and Liu (2006), the $\delta^{34}S_{H_2S}$ calculation factor for chalcopyrite is constant for these temperatures. Type-I and –II chalcopyrite have the $\delta^{34}S_{H_2S}$ values of 0.7 - 0.9 ‰ and 4.3 - 10.4 ‰, respectively. Estimating the precipitation temperature of galena and sphalerite as 200˚C, the $\delta^{34}S_{H_2S}$ values of galena will be 1.6 to 4.7‰ at 200˚C, whereas those of sphalerite range from -3.6 to 2.8‰ (using the data of Li and Liu, 2006).

577 Thus, the source of sulfur for the whole mineralization was uniform and sulfur in the fluid was
578 dominantly H_2S (Shelton et al., 1986; Shelton et al., 1987). The heavier sulfur in the type-I
579 chalcopyrite implies an extraneous sulfur source, probably derived from the country rocks
580 (Kontak, 1990).

581 The $\delta^{34}S_{H_2S}$ values of Panasqueira in Portugal and Pasto Bueno in Peru (-4 to 3 ‰ and -2
582 to 0 ‰, respectively) indicate a magmatic source (Landis and Rye, 1974; Kelly and Rye, 1979;
583 Campbell, 1987). Except for type-I chalcopyrite, the $\delta^{34}S_{H_2S}$ values of Mawchi (-3.6 to 5 ‰) are
584 the same as those of Panasqueira and Pasto Bueno. The heavier sulfur at Mawchi ($\delta^{34}S_{H_2S}$ 4.3 to
585 10.4 ‰) is nearly the same value as San Cristobal ($\delta^{34}S_{H_2S}$ 2 to 9 ‰) of Peru, which also has a
586 major sulfide stage, and magmatic sulfur contaminated with sulfur of sedimentary origin
587 (Campbell, 1987). The source of sulfur for Mawchi is interpreted to be predominantly of magmatic
588 origin, with heavier sulfur in type-I chalcopyrite being probably derived from the country rocks
589 which surround the granite body.

590

591 7.3 *Source of ore fluid*

592 The Sn-W mineralization of Mawchi formed by magmatic-hydrothermal fluids of moderate
593 temperature and low to moderate salinity, very similar to those of Wagone (Myint et al., 2017),
594 Lailishan (Shi et al., 1989 in Cao et al., 2017), Pilok (Linnen and Williams-Jones, 1988),
595 Panasqueira Sn-W deposit, Portugal (Kelly and Rye, 1979), and of the ore forming stage of San

596 Rafael Sn-Cu deposit (Wagner et al., 2009) and Pasto Bueno W base-metal deposit (Landis and
597 Rye, 1974), both in Peru. The ore fluids of the Lailishan, Pilok, Panasqueira, San Rafael and Pasto
598 Bueno were interpreted as a mixture of magmatic and meteoric waters. The early barren stages at
599 San Rafael and Pasto Bueno are characterized by hot (>380˚C) and hypersaline (>34 wt. % NaCl
600 equiv) fluid that can be interpreted as purely magmatic. However, fluids of magmatic origin
601 responsible for the Cleveland tin deposit of Australia (7-14 wt. % NaCl equiv; Collins, 1981) and
602 the Baiganhu District of China (10 - 14 wt. % NaCl equiv; Gao et al., 2014) are not hypersaline.
603 Thus, the early stage, moderate salinity, fluids at Mawchi can be considered as essentially
604 magmatic in origin. By contrast, the later low salinity fluid may have evolved by mixing with
605 either a meteoric or a metamorphic fluid, which is also supported by $\delta^{18}O$ and δD data.

606 The calculated $\delta^{18}O_{H_2O}$ data of cassiterite (7.3 to 8.4 ‰) and tourmaline (7.8 to 8.2 ‰) are
607 consistent with a magmatic source of ore fluid (Taylor, 1974, 1979). At the lower temperature
608 stages, $\delta^{18}O_{H_2O}$ data of wolframite, scheelite and quartz (3.9 to 6.2 ‰, 2.1 to 4.2 ‰ and 3 to 4.9
609 ‰, respectively) are close to being 5 ‰, lower than cassiterite and tourmaline. These lower $\delta^{18}O_{H_2O}$
610 values are again consistent with the view that the ore fluid may have mixed with another source of
611 water, likely of meteoric origin.

612 The oxygen isotope compositional range in cassiterite is small, 5 ± 0.4 ‰, whereas the
613 hydrogen isotope composition ranges from -51 to -98 ‰ (Fig. 12). The fluid with distinctive
614 vertical pattern can have resulted from contamination by a highly evolved meteoric water

615 (Campbell et al., 1984). The fluid inclusions from main ore stage vein minerals (cassiterite,
616 wolframite, quartz) yield δD_{H2O} values from -87 to -51 ‰ implying that the origin of ore fluid is
617 magmatic, as suggested by sulfur. However, the calculated δD_{H2O} value (~ -120‰) of some mineral
618 species (wolframite, tourmaline) is low enough to suggest meteoric contamination in the
619 hydrothermal fluids responsible for the late stage of vein deposition. Although some samples are
620 located in the region of metamorphic water (-65‰ to -20‰ of δD_{H2O} and +5‰ to +25‰ of
621 $\delta^{18}O_{H2O}$), the uniform $\delta^{18}O_{H2O}$ values in same mineral species suggest minor involvement of
622 metamorphic water in the origin of Mawchi ore fluids.

623 The ore forming fluids at Mawchi are a mixture of magmatic and meteoric waters, which
624 implies a water-rock exchange model. The pattern of the fluid compositions, nearly constant
625 $\delta^{18}O_{H2O}$ with a wide range of δD_{H2O}, is very similar to the pattern at Pasto Bueno (Landis and Rye,
626 1974) and San Cristobal, Peru (Campbell et al., 1984; Beuchat et al., 2004) and Panasqueira,
627 Portugal (Kelly and Rye, 1979). This pattern represents an exchange of meteoric waters with the
628 host rocks and the igneous pluton at very low water to rock ratios (<0.05) (Campbell et al., 1984;
629 Shelton et al., 1987).

630

631 7.4 *Ore genesis of Sn-W mineralization in WGP (and TBGP): metallogenic epochs and tectonic*
632 *settings*

633 Geochronological data constrain Sn-W mineralization of the granites in the WGP to the

634 period between the Cretaceous and Eocene. Early Cretaceous (128-121 Ma) granitic rocks in the
635 WGP are represented by I-type magmatism which likely originated from subducted oceanic crust
636 (Barley et al., 2003; Searle et al., 2007) and lack associated with Sn-W mineralization. The oldest
637 tin bearing pegmatite of the WGP has been dated from Mawpalaw Taung at 106.8±1.6Ma (Paik
638 and Zaw, 2014) Younger Cretaceous tin granites from the WGP have been identified at Xiaolonghe
639 (73 Ma; Chen et al., 2015) and also at Pilok (72 Ma Ar-Ar biotite date; Charusiri et al., 1993). U-
640 Pb zircon data yielded 61.44 ± 0.62 Ma and 61.38 ± 0.54 Ma for the Hermyingyi granite and
641 Wagone granirespectively (Li et al., under review), collectively suggesting that wide-spread
642 emplacement of tin granites in the WGP occurred in the late Cretaceous and Paleocene. Biotite K-
643 Ar dating yielded an Earliest Eocene age of 55 ± 1 Ma for the Padatchaung granite (Brook and
644 Snelling, 1976) and, U-Pb zircon dating yielded for Lailishan, 52.7 ± 0.3 – 53.0 ± 0.4 Ma (Chen
645 et al., 2015) and for Yadanabon, 50.3 ± 0.6 Ma (Gardiner et al., 2016), respectively. The 42 Ma
646 LA-ICP-MS zircon U-Pb ages coupled with 41.5 ± 0.2 Ma biotite Ar-Ar age of Mawchi granites
647 affirms Late Eocene tin granite emplacement in WGP and is the youngest age for tin mineralization
648 in the province. In the MMB west of the SB, S-type granites range from 72 Ma to 44 Ma and lack
649 significant tin mineralization.

650 The tin granites of WGP were derived from the partial melting of the crust (Gardiner et al.,
651 2016; Myint et al., 2017a&b) and the emplacement of these granites has been variously related to
652 the Cretaceous–Paleogene subduction- and Himalayan orogeny-related collision (Gardiner et al.,

2015), back-arc extension, or post-collisional or syncollisional extension related granitic magmatism (Chen et al., 2015; Jiang et al., 2017; Myint et al. 2017a; Chen et al., 2018). Interpretation of some WGP granites as A-2 type and derived from partial melts of Proterozoic intrusions is also proposed (Jiang et al., 2017). Triassic to Jurassic CGP tin granites related to the Sibumasu - Sukhothai arc collision form the older Asian tin belt while collisional and post-collisional Cretaceous to Eocene WGP tin bearing granites formed a younger belt before, during and after the India – Asia collision. Assimilation of the crust (eg. SB in WGP; Kontum massif in CGP) led to the production of highly siliceous and highly fractionated tin granites (Chen et al., 2018; Ng et al., 2015a; Myint et al. 2017a&b).

8. Conclusions

The Mawchi Sn-W polymetallic deposit consists of a suite of Sn-W sulfide veins with minor skarn and stockworks. Three stages of ore deposition were recognized, namely (1) the tourmaline-cassiterite stage, (2) the main ore stage and (3) the sulfide stage. Tourmaline, cassiterite, muscovite and pyrite-I are minerals that formed early in the hydrothermal activity and their deposition occurred in the granite body. Wolframite, scheelite, arsenopyrite, pyrite-II, molybdenite, fluorite, chlorite, danalite and calcite formed during the main ore stage together with the products formed earlier. Sulfide minerals such as chalcopyrite, sphalerite, galena and Pb-Bi sulfides were deposited during the termination of the mineralization with hydrothermal activity

672 continuing substantially after deposition of the metals.

673 Our study provides the first isotopic age determination of Sn-W mineralization in
674 Myanmar. Combining new Ar-Ar geochronological data with previous U-Pb zircon data constrains
675 the magmatic-hydrothermal activity at Mawchi to a short time span that implies successive ore
676 deposition and magmatism. The biotite granite at Mawchi was emplaced and crystallized at 43-42
677 Ma with coeval magmatic-hydrothermal activity resulting in precipitation of the mineralization
678 paragenesis over a period of around 1-2 million years. Successive hydrothermal activity
679 transformed part of the biotite granite to tourmaline granite by adding tourmaline and muscovite
680 of hydrothermal origin. At the same time, cassiterite deposition together with tourmalinization
681 took place in veins emplaced along the fractures in the granite. Muscovite-sericite Ar-Ar data of
682 vein quartz constrains the late stage of mineralization at Mawchi to around 41 Ma.

683 The proposed deposit model is based on the stable isotope and fluid inclusion data.
684 Homogenization temperatures range from 175˚ to 340˚C for the Mawchi vein system. This
685 relatively moderate temperature, moderate salinity brine (≤15 equiv. wt. % NaCl) ore fluid was
686 originally produced by magmatic water and probably mixed with meteoric water later during
687 circulation through adjacent metasediments. However, the sulfur was relatively uniform
688 throughout the hydrothermal activity, and likely purely magmatic derived except for the sulfur in
689 type-I chalcopyrite which was contaminated with sulfur from country rocks. In conclusion, the
690 hydrothermal fluids of Mawchi were derived from the mixing of magmatic and meteoric waters.

Acknowledgements

Sincere thanks are due to the Japan International Cooperation Agency (JICA) for the PhD scholarship for AZM and Global COE Program of Kyushu University for support for the field work. The Society of Economic Geologists Foundation is thanked for their student research grant to AZM. We would like to thank Alison McDonald and Julie Dougan from SUERC, UK for their valuable assistance during stable isotopic experiments. EPMA analysis was supported by Professor Yasuhito Osanai and Dr. Tatsuro Adachi from Kyushu University. We are deeply appreciated to two reviewers for their critical reading of manuscript and providing valuable comments. Special thanks are also due to Kayah Metal Production Co. Ltd and Ye Htut Kyaw Mining Co. Ltd for generously providing the first author an office space to work in and for providing logistical support. DS acknowledges the Total Endowment Fund.

REFERENCES

Barley, M. E., Pickard, A. L., Zaw, K., Rak, P., Doyle, M. G., 2003. Jurassic to Miocene magmatism and metamorphism in the Mogok metamorphic belt and the India-Eurasia collision in Myanmar. Tectonics, 22, 3, 10-19.

Bender, F. 1983. Geology of Burma, Gebruder Borntraeger, Berlin, Stuttgart.

Beuchat, S., Moritz, R., Pettke, T., 2004. Fluid evolution in the W–Cu–Zn–Pb San Cristobal vein, Peru: fluid inclusion and stable isotope evidence. Chem. Geol. 210, 201–224.

711 Blamart, D., 1991. Les concentrations tungstifères et stannifères: caractérisation isotopique(O-H) des fluides
712 minéralisateurs, sur l'exemple du gisement Sn-W de Walmès(Maroc Central)". Détermination de quelques
713 fractionnements isotopiques(H-O) entre minéraux et eau. unpublished Doctoral dissertation, Institut National
714 Polytechnique de Lorraine, France.
715 Brook, M., Snelling, N.J., 1976. K/Ar and Rb/Sr age determinations on rocks and minerals from Burma. London, Inst.
716 Geol. Sci. Isotope Geol. Unit Rep. 76/12
717 Campbell, A.R., 1987. A sulfur isotopic study of the San Cristobal tungsten-base metal mine, Peru. Miner.
718 Deposita. 22, 42–46.
719 Campbell, A.R., Rye, D., Petersen, U., 1984. A hydrogen and oxygen isotope study of the San Cristobal Mine, Peru;
720 implications of the role of water to rock ratio for the genesis of wolframite deposits. Econ. Geol. 79, 1818–
721 1832.
722 Cao, H. W., Pei, Q. M., Zhang, S. T., Zhang, L. K., Tang, L., Lin, J. Z., Zheng, L., 2017. Geology, geochemistry and
723 genesis of the Eocene Lailishan Sn deposit in the Sanjiang region, SW China. J. Asian Earth Sci., 137, 220-
724 240.
725 Cao, H.W., Zou, H., Zhang, Y.H., Zhang, S.T., Zheng, L., Zhang, L.K., Tang, L., Pei, Q.M., 2016. Late Cretaceous
726 magmatism and related metallogeny in the Tengchong area: Evidence from geochronological, isotopic and
727 geochemical data from the Xiaolonghe Sn deposit, western Yunnan, China. Ore Geol Rev, 78, 196-212.
728 Charusiri, P., Clark, A.H., Farrar, E., Archibald, D., Charusiri, B., 1993. Granite belts in Thailand: evidence from the
729 40 Ar/39 Ar geochronological and geological syntheses. J. Southeast Asian Earth Sci., 8, 127-136.

730 Chen, X.C., Hu, R.z., Bi, X.W., Zhong, H., Lan, J.B., Zhao, C.H., Zhu, J.J., 2015. Petrogenesis of metaluminous A-
731 type granitoids in the Tengchong–Lianghe tin belt of southwestern China: evidence from zircon U–Pb ages and
732 Hf–O isotopes, and whole-rock Sr–Nd isotopes. Lithos, 212–215, 93–110.
733 Chen, X.C., Zhao, C.H., Zhu, J.J., Wang, X.S. and Cui, T., 2018. He, Ar, and S isotopic constraints on the relationship
734 between A-type granites and tin mineralization: A case study of tin deposits in the Tengchong–Lianghe tin belt,
735 southwest China. Ore Geol. Rev., 92, 416-429.
736 Chhibber, D.H.L., 1934. The geology of Burma. Macmillan, London.
737 Clegg, E.L.G., 1944. Notes on tin and wolfram in Burma and India. Rec. Geol. Surv. India 76, 168p .
738 Cobbing, E.J., Pitfield, P.E.J., Darbyshire, D.P.F., Mallick, D.I.J., 1992. The granites of the South-East Asian tin belt.
739 Overseas Memoir British Geol. Surv. 10, 369 p.
740 Collins, P.L.F., 1981. The geology and genesis of the Cleveland tin deposit, western Tasmania; fluid inclusion and
741 stable isotope studies. Econ. Geol. 76, 365–392 .
742 Dalrymple, G.B., Lanphere, M.A., 1971. A test of the $^{40}Ar/^{39}Ar$ age spectrum technique on some terrestrial
743 materials. Earth Planet. Sci. Lett. 12, 359–372.
744 DGSE (Department of Geological Survey and Mineral Exploration), 2008. Geological Map of the Union of Myanmar.
745 Dunn, J.A., 1938. Tin-tungsten mineralization at Mawchi, Karenni States, Burma. Rec. Geol. Surv. India 73, 238–
746 246.
747 Eby, G.N., 1992. Chemical subdivision of the A-type granitoids: petrogenetic and tectonic implications. Geology 20,
748 641–644.

749 Fallick, A.E., McConville, P., Boyce, A.J., Burgess, R., Kelley, S.P., 1992. Laser microprobe stable isotope
750 measurements on geological materials: some experimental considerations (with special reference to $\delta^{34}S$ in
751 sulfides). Chem. Geol. 101, 53–61.
752 Gao, Y., Li, W., Li, Z., Wang, J., Hattori, K., Zhang, Z., Geng, J., 2014. Geology, geochemistry, and genesis of
753 tungsten-tin deposits in the Baiganhu district, northern Kunlun belt, northwestern China. Econ. Geol. 109,
754 1787–1799.
755 Gardiner, N.J., Robb, L.J., Morley, C.K., Searle, M.P., Cawood, P.A., Whitehouse, M.J., Kirkland, C.L., Roberts,
756 N.M.W., Myint, T.A., 2016. The tectonic and metallogenic framework of Myanmar: A Tethyan mineral system.
757 Ore. Geol. Rev., 79, 26-45.
758 Gardiner, N.J., Searle, M.P., Robb, L.J., Morley, C.K., 2015. Neo-Tethyan magmatism and metallogeny in Myanmar–
759 An Andean analogue? J. Asian Earth Sci. 106, 197–215.
760 Grootenboer, J., Schwarcz, H.P., 1969. Experimentally determined sulfur isotope fractionations between sulfide
761 minerals. Earth Planet. Sci. Lett. 7, 162–166.
762 Hermansson, T., Stephens, M.B., Corfu, F., Page, L.M., Andersson, J., 2008. Migratory tectonic switching, western
763 Svecofennian orogen, central Sweden: constraints from U/Pb zircon and titanite geochronology. Precamb.
764 Res. 161, 250–278.
765 Hobson, G.V., 1940. The development of the mineral deposit at Mawchi as determined by its geology and genesis.
766 Transactions of the Mines, Geol. Metal. Inst. India 36, 35–78.
767 Hobson, G.V., 1941. Report on a geological survey in part of Karenni and Southern Shan States. Mem. Geol. Surv.
768 India 74, 103–155.
769 Htay, H., Lwin, M., Tun, H., Win, A.N., Win, K.M., 1997. Preliminary report on re-assessment of ore reserves at the

Mawchi mines, Phasawng Township, Kayah State. unpublished Report, Ministry of Mines, Myanmar

Iyer, L.A.N., 1953. The geology and gem-stones of the Mogok Stone Tract, Burma. Geol. Surv. India Mem. 82, 100p.

Jiang, H., Li, W.Q., Jiang, S.Y., Wang, H. and Wei, X.P., 2017. Geochronological, geochemical and Sr-Nd-Hf isotopic constraints on the petrogenesis of Late Cretaceous A-type granites from the Sibumasu Block, Southern Myanmar, SE Asia. Lithos, 268, 32-47.

Kelley, S.P., Fallick, A.E., 1990. High precision spatially resolved analysis of $\delta^{34}S$ in sulfides using a laser extraction technique. Geochim. Cosmochim. Acta 54, 883–888.

Kelly, W.C., Rye, R.O., 1979. Geologic, fluid inclusion, and stable isotope studies of the tin-tungsten deposits of Panasqueira, Portugal. Econ. Geol. 74, 1721–1822.

Kohút, M., Recio, C., 2002. Sulphur isotopes of selected Hercynian granitic and surrounding rocks from the Western Carpathians (Slovakia). Geol. Carpathica 53, 3–13.

Kontak, D.J., 1990. A sulfur isotope study of main-stage tin and base metal mineralization at the East Kemptville tin deposit, Yarmouth County, Nova Scotia, Canada; evidence for magmatic orgin of metals and sulfur. Econ. Geol. 85, 399–407.

Landis, G.P., Rye, R.O., 1974. Geologic, fluid inclusion, and stable isotope studies of the Pasto Buena tungsten-base metal ore deposit, Northern Peru. Econ. Geol. 69, 1025–1059.

Li, H., Myint, A.Z., Yonezu, K., Watanabe, K., Algeo, T.J., Wu, J-H, (under review) Geochemistry and U–Pb geochronology of the Wagone and Hermyingyi granites, Dawei region, southern Myanmar: Implications for tectonic setting, magma evolution and Sn–W mineralization

Li, Y., Liu, J., 2006. Calculation of sulfur isotope fractionation in sulfides.Geochim. Cosmochim. Acta 70, 1789–1795.

Mitchell, A.H.G., 1977. Tectonic settings for emplacement of Southeast Asian tin granites. Geological Society of Malaysia Bulletin 9, 123–140.

793 Mitchell, A.H.G., Ausa, C., Deiparine, L., Hlaing, T., Htay, N., Khine, A., 2004. The Modi Taung-Nankwe gold
794 district, Slate Belt, Central Myanmar: mesothermal veins in a Mesozoic orogen. J. Asian Earth Sci. 23, 321–
795 341.
796 Mitchell, A.G.H., Htay, M.T., Htun, K.M., Win, M.N., Oo, T., 2007. Rock relationships in the Mogok metamorphic
797 belt, Tatkon to Mandalay, Central Myanmar. J. Asian Earth Sci. 29, 891–910.
798 Mitchell, A.H.G., Chung, S-L., Oo, T., Lin, T-H., Hung, C-H., 2012. Zircon U–Pb ages in Myanmar: Magmatic–
799 metamorphic events and the closure of a neo-Tethys ocean? J. Asian Earth Sci. 56, 1–23.
800 Myint, A.Z., 2015. Granite-related Sn-W-REE mineralization in Mawchi and Dawei areas, Myanmar. unpublished
801 PhD Dissertation, Kyushu University.
802 Myint, A.Z., Watanabe, K., Yonezu, K., 2013. Relationship between granitoid types and tin mineralization: A review
803 of Tertiary granitoids in central granitoid belt, Myanmar. Proceedings of International Conference on
804 Georesources and Geological Engineering, Yogyakarta, Indonesia. pp 13–21.
805 Myint, A.Z., Zaw, K., Swe, Y.M., Yonezu, K., Cai, Y., Manaka, T., Watanabe, K., 2017a. Geochemistry and
806 geochronology of granites hosting the Mawchi Sn-W deposit, Myanmar: Implication for tectonic setting and
807 granite emplacement. In: Barber AJ, Khin Zaw & Crow MJ (ed) Myanmar: Geology, Resources and
808 Tectonics. Geol. Soc. Lond. Memoir 48, pp 387–402.
809 Myint, A.Z., Yonezu, K., Watanabe, K., 2017b. The tin and tungsten deposits of the Dawei region, with an emphasis
810 on the Wagone and Bawapin deposits. In: Mineral deposits of Myanmar (Burma). SEG guide book 54. pp
811 22–27.
812 Ng, S. W-P., Chung, S-L., Robb, L.J., Searle, M.P., Ghani, A.A., Whitehouse, M.J., Oliver, G.J.H., Sone, M.,
813 Gardiner, N.J., Roselee, M.H., 2015a. Petrogenesis of Malaysian granitoids in the Southeast Asian tin belt:
814 Part 1. Geochemical and Sr-Nd isotopic characteristics. GSA Bull. 127, 1209–1237.

815 Ng, S. W-P., Whitehouse, M.J., Searle, M.P., Robb, L.J., Ghani, A.A., Chung, S-L., Oliver, G.J.H., Sone, M.,
816 Gardiner, N.J., Roselee, M.H., 2015b. Petrogenesis of Malaysian granitoids in the Southeast Asian tin belt:
817 Part 2. U-Pb zircon geochronology and tectonic model. GSA Bull. 127, 1238–1258.
818 Ohmoto, H., Rye, R.O., 1979. Isotopes of sulfur and carbon. In: Barnes HL (ed) Geochemisty of hydrothermal ore
819 deposits. New York, Wiley, pp 509–567.
820 Paik, M., Zaw, K., 2014. Age, petrology and geochemistry of granitoid rocks in Mawpalaw Taung Area, Thanbyuzayat
821 Township: Constraints on their magmagenesis and tectonic Setting. Abstract Volume, Thirteenth Regional
822 Congress on Geology, Mineral and Energy Resources of Southeast Asia, Yangon, Myanmar.
823 Renne, P.R., Swisher, C.C., Deino, A.L., Karner, D.B., Owens, T., Depaolo, D.J., 1998. Intercalibration of Standards,
824 absolute ages and uncertainties in 40Ar/39Ar dating. Chem. Geol. 145, 117–152.
825 Robinson, B.W., Kusakabe, M., 1975. Quantitative preparation of sulfur dioxide, for sulfur-34/sulfur-32 analyses,
826 from sulfides by combustion with cuprous oxide. Analyt. Chem. 47, 1179–1181.
827 Schwartz, M. O., Rajah, S. S., Askury, A. K., Putthapiban, P., Djaswadi, S., 1995. The southeast Asian tin belt. Earth-
828 Science Reviews, 38, 95-293.
829 Searle, D.L., Haq, B.T., 1964. The Mogok belt of Burma and its relationship to the Himalayan orogeny. In:
830 Proceedings of the 22nd International Geological Conference, Delhi, 11, pp 132–161.
831 Searle, M. P., Noble, S. R., Cottle, J. M., Waters, D. J., Mitchell, A. H. G., Hlaing, T., Horstwood, M. S. A., 2007.
832 Tectonic evolution of the Mogok metamorphic belt, Burma (Myanmar) constrained by U - Th - Pb dating of
833 metamorphic and magmatic rocks. Tectonics, 26
834 Selby, D., Creaser, R.A., 2001. Late and mid-Cretaceous mineralization in the northern Canadian Cordillera:
835 Constraints from Re-Os molybdenite dates. Econ. Geol. 96, 1461–1467.

836 Selby, D., Creaser, R.A., Stein, H.J., Markey, R.J., Hannah, J.L., 2007. Assessment of the 187 Re decay constant by
837 cross calibration of Re–Os molybdenite and U–Pb zircon chronometers in magmatic ore systems. Geochim.
838 Cosmochim. Acta 71, 1999–2013.
839 Shelton, K.L., So, C.S., Rye, D.M., Park, M.E., 1986. Geologic, sulfur isotope, and fluid inclusion studies of the
840 Sannae W-Mo Mine, Republic of Korea; comparison of sulfur isotope systematics in Korean W deposits. Econ.
841 Geol. 81, 430–446.
842 Shelton, K.L., Taylor, R.P., So, C.S., 1987. Stable isotope studies of the Dae Hwa tungsten-molybdenum mine,
843 Republic of Korea; evidence of progressive meteoric water interaction in a tungsten-bearing hydrothermal
844 system. Econ. Geol. 82, 471–481.
845 Smoliar, M.I., Walker, R.J., Morgan, J.W., 1996. Re-Os ages of group IIA, IIIA, IVA, and IVB iron
846 meteorites. Science 271, 1099–1102.
847 Taylor, H.P., 1974. The application of oxygen and hydrogen isotope studies to problems of hydrothermal alteration
848 and ore deposition. Econ. Geol. 69, 843–883.
849 Taylor, H.P., 1979. Oxygen and hydrogen isotope relationships in hydrothermal mineral deposits. In: Barnes HL (ed)
850 Geochemisty of hydrothermal ore deposits. New York, Wiley, pp 236–277
851 Taylor, R.P., Ikingura, J.R., Fallick, A.E., Huang, Y., Watkinson, D.H., 1992. Stable isotope compositions of
852 tourmalines from granites and related hydrothermal rocks of the Karagwe-Ankolean belt, northwest
853 Tanzania. Chem. Geol. 94,215–227
854 Thein, M., 1991. Mineral belts and epoches of Myanmar: A new synthesis. Georeport 1, 1–10.
855 Thein, M.L., Myint, O., Kyi, S., 1988. Geology and stratigraphy of the metamorphosed early Palaeozoic rocks of the
856 Thabeikkyin- Mogok areas. unpublished report, Applied Geology Department, University of Rangoon,57 p.
857 United Nations, 1996. Geology and Mineral Resources of Myanmar. Atlas of mineral resources of the ESCAP region
858 12.

Wagner, T., Boyce, A.J., Fallick, A.E., 2002. Laser combustion analysis of $\delta^{34}S$ of sulfosalt minerals: determination of the fractionation systematics and some crystal-chemical considerations. Geochim. Cosmochim. Acta 66, 2855–2863.

Wagner, T., Mlynarczyk, M.S., Williams-Jones, A.E., Boyce, A.J., 2009. Stable isotope constraints on ore formation at the San Rafael tin-copper deposit, Southeast Peru. Econ. Geol. 104, 223–248.

Wagner, T., Williams-Jones, A.E., Boyce, A.J., 2005. Stable isotope-based modeling of the origin and genesis of an unusual Au–Ag–Sn–W epithermal system at Cirotan, Indonesia. Chem. Geol. 219, 237–260.

Wang, C., Deng, J., Carranza, E.J.M., Santosh, M., 2014. Tin metallogenesis associated with granitoids in the southwestern Sanjiang Tethyan Domain: Nature, deposit types, and tectonic setting. Gondwana Res., 26, 576-593.

Wesolowski, D., Ohmoto, H., 1986. Calculated oxygen isotope fractionation factors between water and the minerals scheelite and powellite. Econ. Geol. 81, 471–477.

Whalen, J.B., Currie, K.L., Chappell, B.W., 1987. A-type granites: geochemical characteristics, discrimination and petrogenesis. Cont. Min. Pet. 95, 407–419.

Zaw K, Thet KM (1983) A note on a fluid inclusion study of tin-tungsten mineralization at Mawchi Mine, Kayah State, Burma. Econ Geol 78:530–534

Zhang, L-G., Liu, J., Chen, Z., Zhou, H., 1994. Experimental investigations of oxygen isotope fractionation in cassiterite and wolframite. Econ. Geol. 89, 150–157.

Zheng, Y.F., 1993. Calculation of oxygen isotope fractionation in hydroxyl-bearing silicates. Earth Planet. Sci. Lett. 120, 247–263.

Figure captions

Fig. 1 a Granitoid belts of Myanmar and its adjacent area showing the occurrences of granites and tectonic framework (modified after Cobbing et al., 1992; Mitchell et al., 2007; Sone and Metcalfe, 2008). **b** Regional geologic setting of the Mawchi area (modified after Bender, 1983; DGSE, 2008)

Fig. 2 a Geological map of Mawchi Sn-W district showing the localities of Sn-W mineral systems. **b** Deposit geological map and vertical profile of Mawchi mine (modified after Mawchi mine project map)

Fig. 3 a quartz vein cutting the granite body: intensive tourmalinization along the contact between vein and host rock. **b** small sheeted veins intruding the metasediments. **c** danalite(da) boundary vein hosted by the granite(gr). **d** later formed quartz-tourmaline barren vein. **e** vein boundary segregates of wolframite (bladed) and cassiterite. **f** fracture filling of quartz and cassiterite. **g** hand specimen collected from massive band of cassiterite with minor amount of tourmaline and clay minerals. **h** hydrothermal muscovite (mu) in fractures of tourmaline (tu)

Fig. 4 Paragenetic sequence of Mawchi Sn-W polymetallic mineralization

Fig. 5 Photomicrographs (**a-f, h**) and hand specimen (**g**) showing the mineral distribution of Mawchi veins. **a** cassiterite (ca) cross cut by wolframite (wf) and, replaced and veined by pyrite-II (py-II). **b** kinked molybdenite (mo) replaced by pyrite-II (py-II): small chalcopyrite blebs (cp) replaced in pyrite. **c** zoned cassiterite crystal. **d** cassiterite veined and replaced by wolframite: wolframite replaced by pyrite-II. **e** cleavage planes of wolframite replaced by scheelite (sh). **f** pyrite-I cubes replaced by arsenopyrite (ap) and pyrite-II which is veined by chalcopyrite (cp). **g** scheelite crystal (milky white) associated with cassiterite and wolframite. **h** tourmaline inclusions in scheelite crystal

Fig. 6 a interstitial filling of pyrite-II into wolframite grains. **b** greenish fluorite and cassiterite in the vein. **c** parallel flow of wolframoixiolites. **d** pyrite-II replaced by sphalerite (sp) and

chalcopyrite (cp); sphalerite hosts the blebs of chalcopyrite and stannite (st) forming as exsolution pattern. **e** type-II chalcopyrite (cp) and pyrite-II, as infill veinlets along fractures of arsenopyrite (ap). **f** pyrite-II (py-II) replaced by type-I chalcopyrite (cp). **g** sphalerite (sp) replaced and veined by galena. **h** pyrite-II (py-II) and chalcopyrite (cp) replaced by the Pb-Bi sulfide

Fig. 7 $^{40}Ar/^{39}Ar$ plateau and inverse isochron ages (2σ) for micas from Mawchi

Fig. 8 Histograms of homogenization temperatures of fluid inclusions in vein minerals of the Mawchi mine

Fig. 9 Salinity variation of fluid inclusions in vein minerals from the Mawchi mine

Fig. 10 The $\delta^{34}S$ values of sulfides from the Mawchi mine. Numbers of analyses in parentheses

Fig. 11 The calculated $\delta^{18}O_{H_2O}$ values of ore fluid from the Mawchi mine

Fig. 12 Plot of $\delta^{18}O$-δD of vein minerals from the Mawchi Sn-W polymetallic deposit (modified from Taylor, 1974)

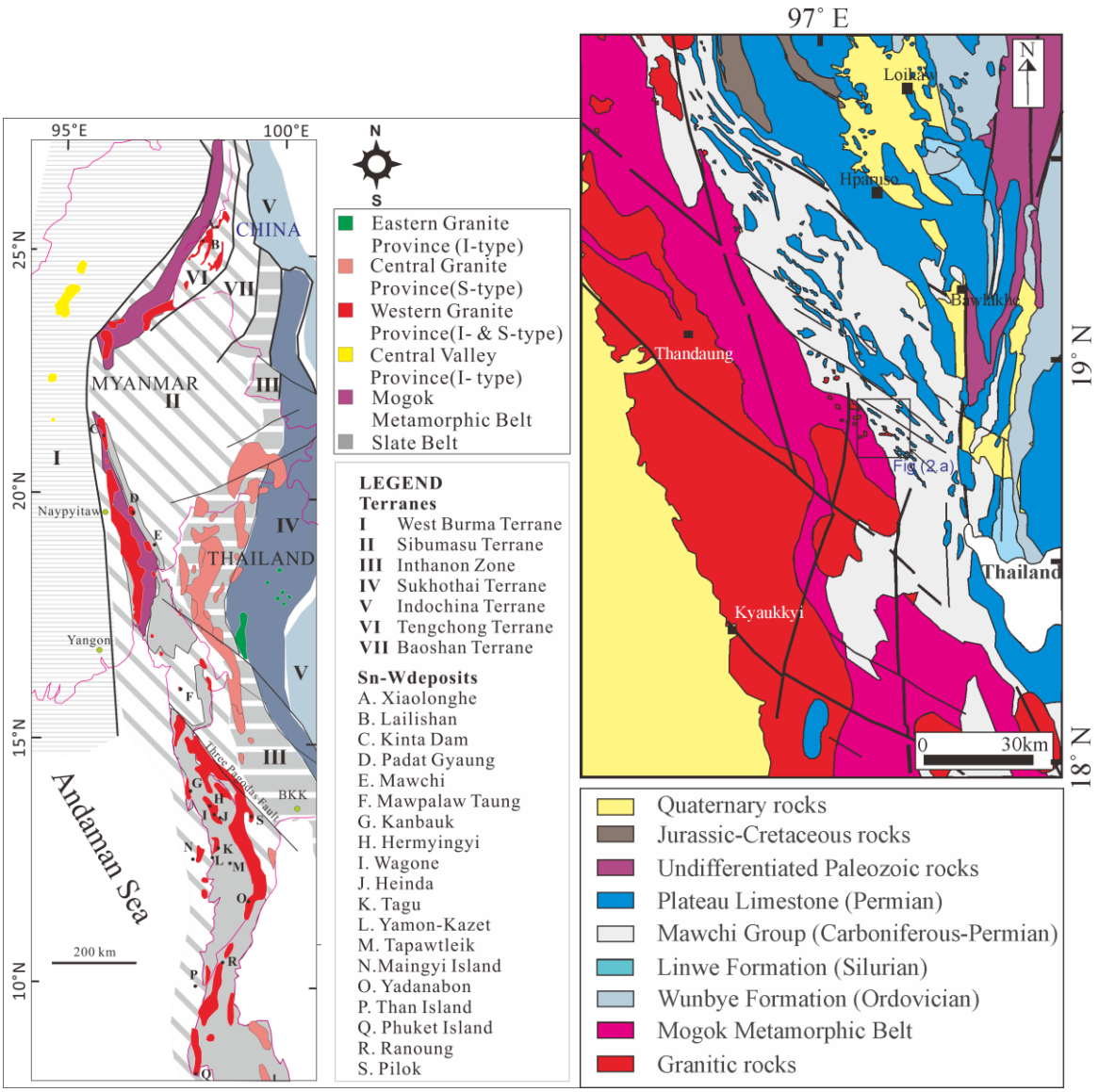
95°E
100°E
25°N
20°N
15°N
10°N
MYANMAR
II
CHINA
V
VI
VII
III
I
IV
THAILAND
V
III
Naypyitaw
Yangon
BKK
Andaman Sea
Three Pagodas Fault
200 km
N
S
Eastern Granite Province (I-type)
Central Granite Province(S-type)
Western Granite Province(I- & S-type)
Central Valley Province(I- type)
Mogok Metamorphic Belt
Slate Belt
LEGEND
Terranes
I West Burma Terrane
II Sibumasu Terrane
III Inthanon Zone
IV Sukhothai Terrane
V Indochina Terrane
VI Tengchong Terrane
VII Baoshan Terrane
Sn-Wdeposits
A. Xiaolonghe
B. Lailishan
C. Kinta Dam
D. Padat Gyaung
E. Mawchi
F. Mawpalaw Taung
G. Kanbauk
H. Hermyingyi
I. Wagone
J. Heinda
K. Tagu
L. Yamon-Kazet
M. Tapawtleik
N.Maingyi Island
O. Yadanabon
P. Than Island
Q. Phuket Island
R. Ranoung
S. Pilok
97° E
19° N
18° N
Loikaw
Hpa-an
Bawlakhe
Thandaung
Fig (2,a)
Thailand
Kyaukkyi
N
0
30km
Quaternary rocks
Jurassic-Cretaceous rocks
Undifferentiated Paleozoic rocks
Plateau Limestone (Permian)
Mawchi Group (Carboniferous-Permian)
Linwe Formation (Silurian)
Wunbye Formation (Ordovician)
Mogok Metamorphic Belt
Granitic rocks

Fig (1)

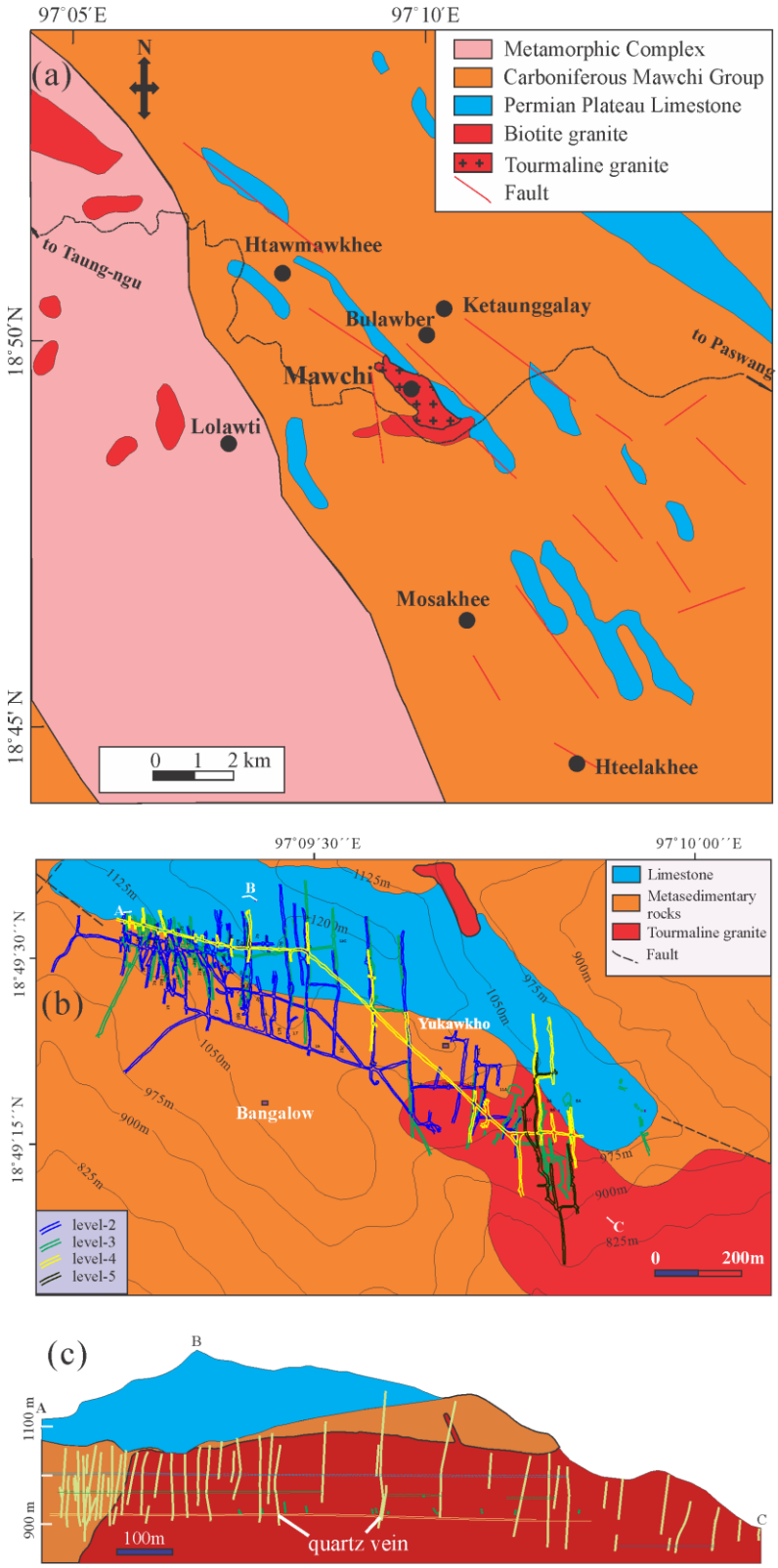

927

928 Fig (2)

929

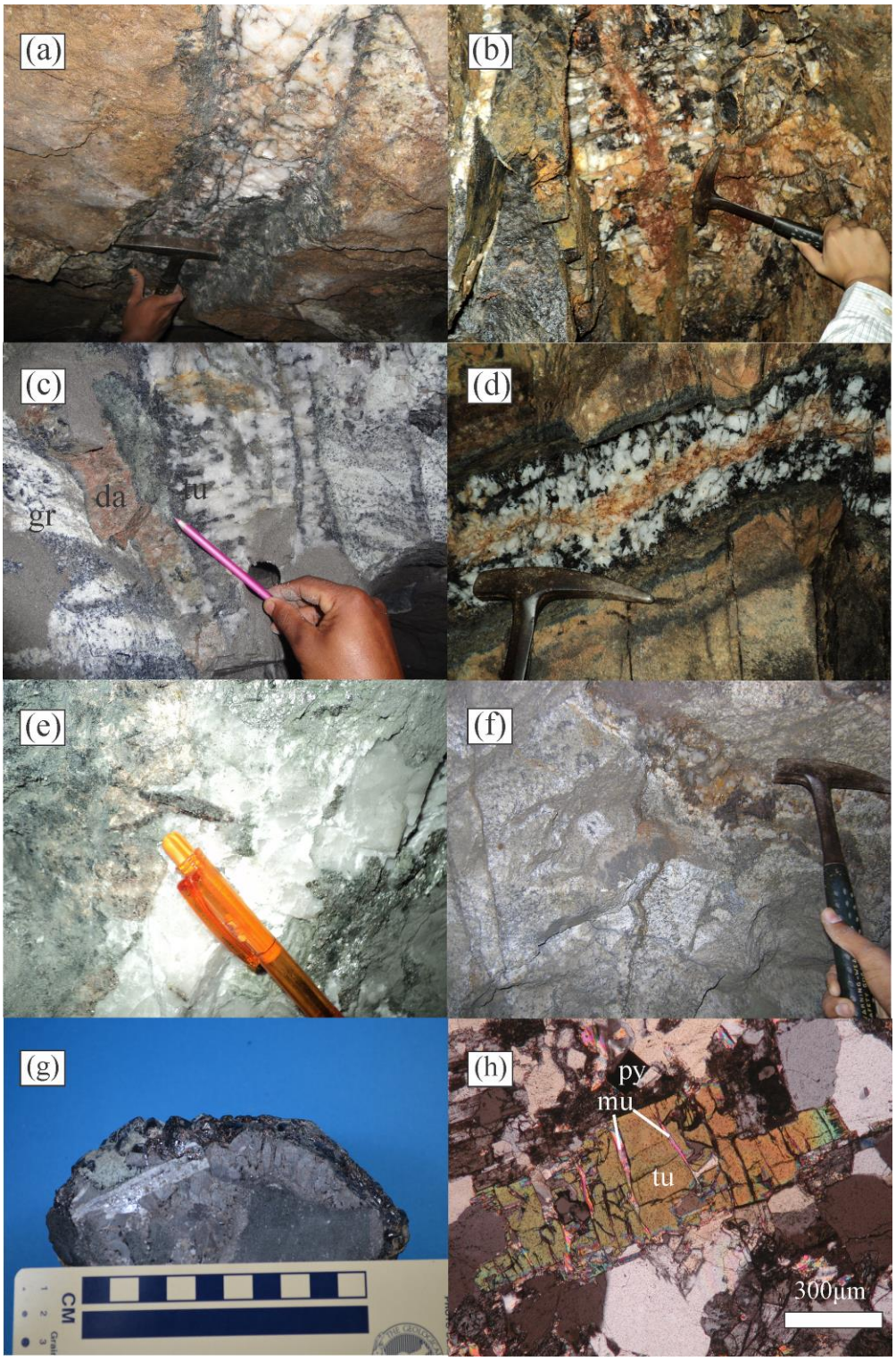

Fig (3)

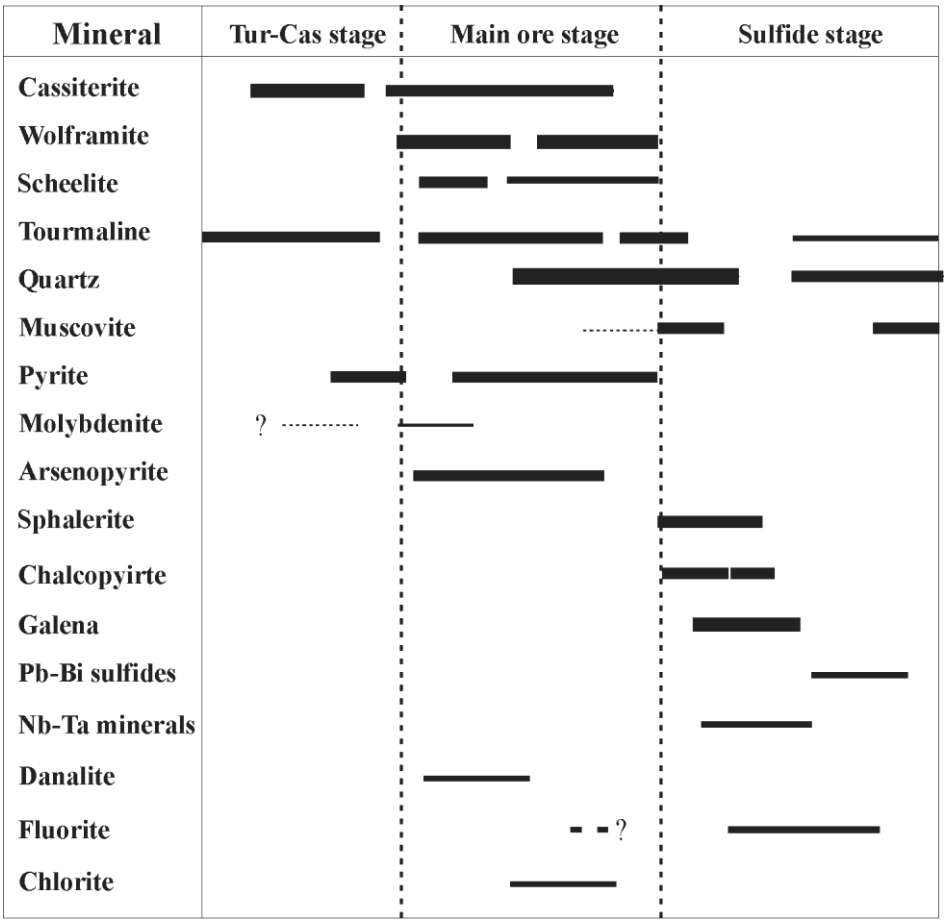
Mineral
Tur-Cas stage
Main ore stage
Sulfide stage
Cassiterite
Wolframite
Scheelite
Tourmaline
Quartz
Muscovite
Pyrite
Molybdenite
?
Arsenopyrite
Sphalerite
Chalcopyirte
Galena
Pb-Bi sulfides
Nb-Ta minerals
Danalite
Fluorite
?
Chlorite

Fig (4)

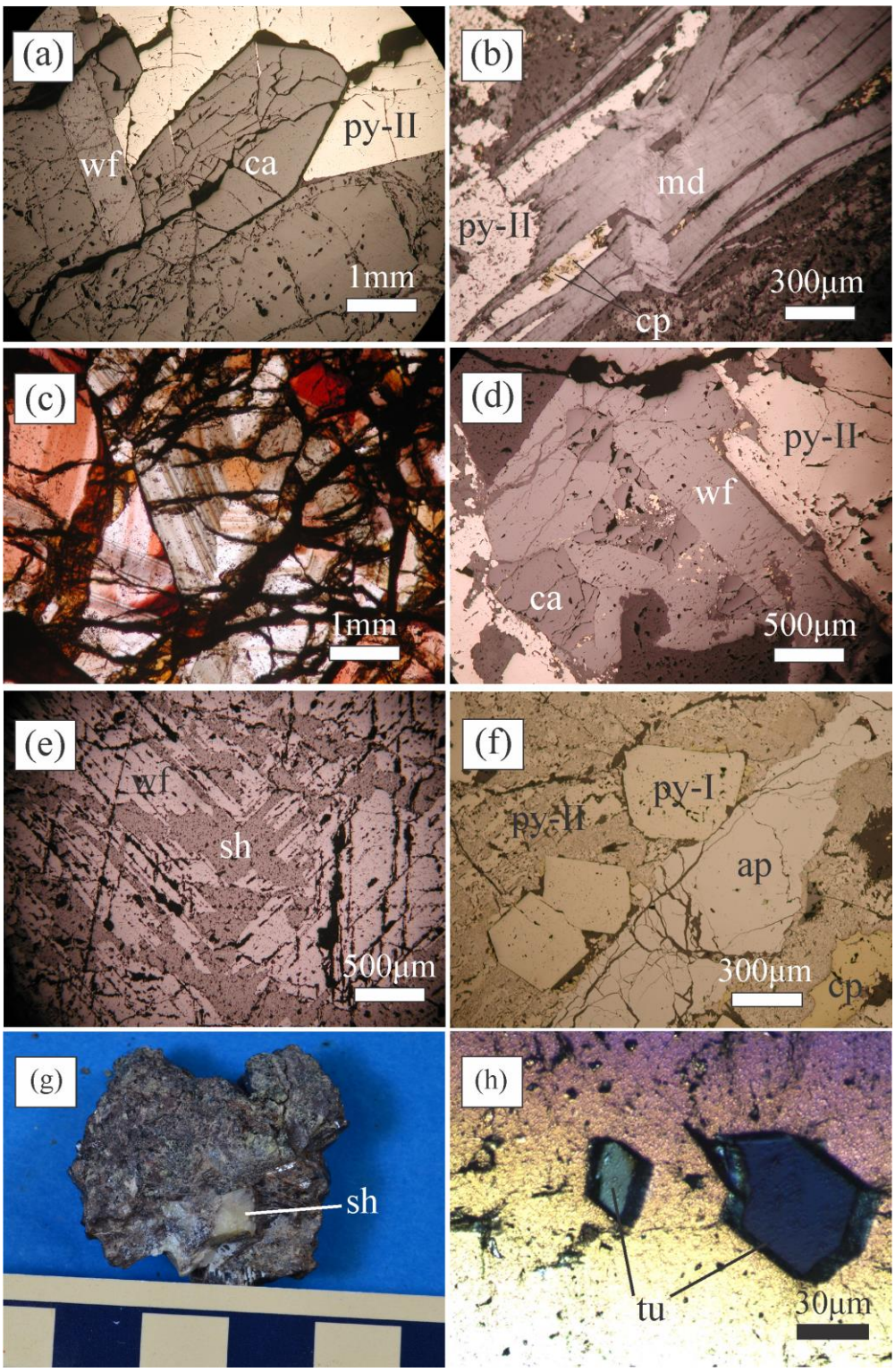

944

945 Fig (5)

946

947

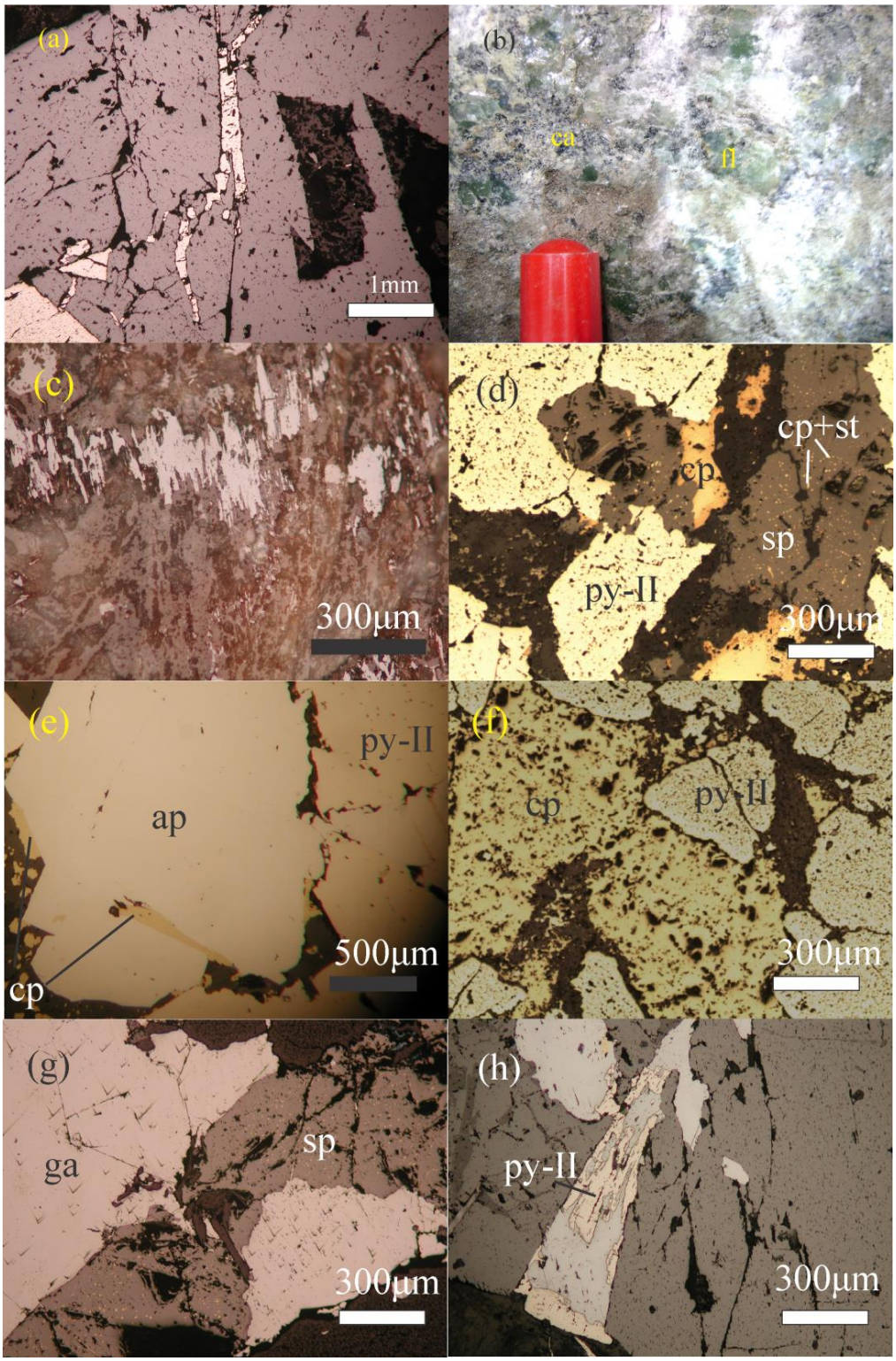

948

949 Fig (6)

950

951

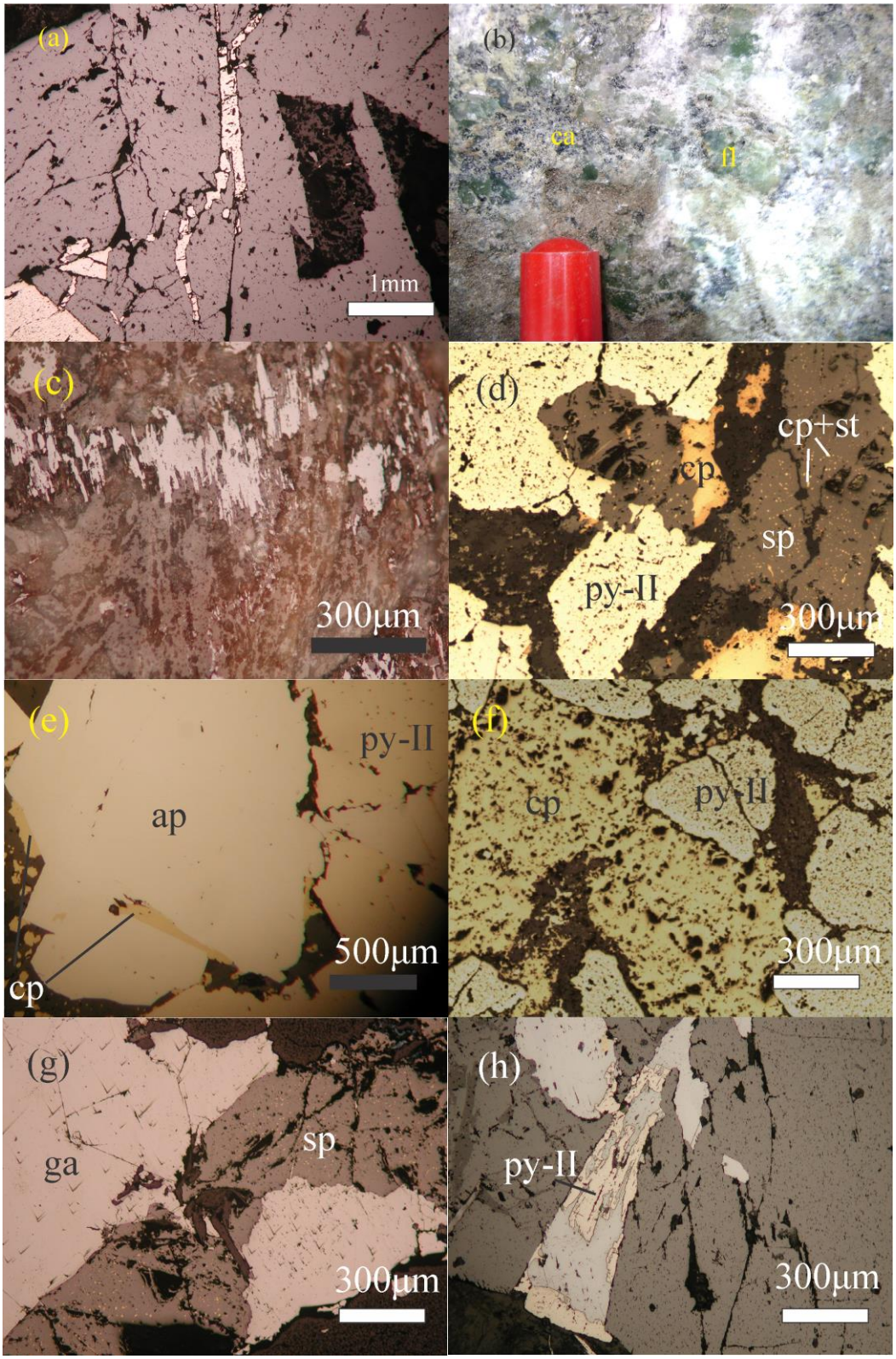

952

953 Fig (7)

954

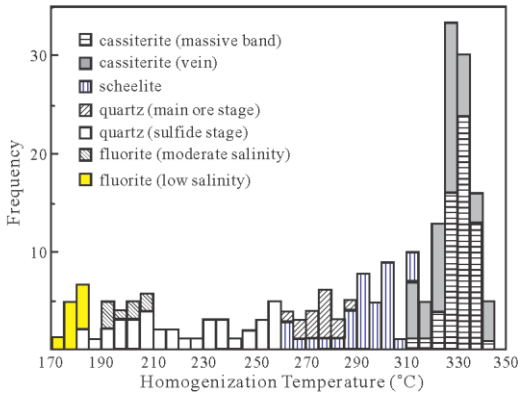

955

956 Fig (8)

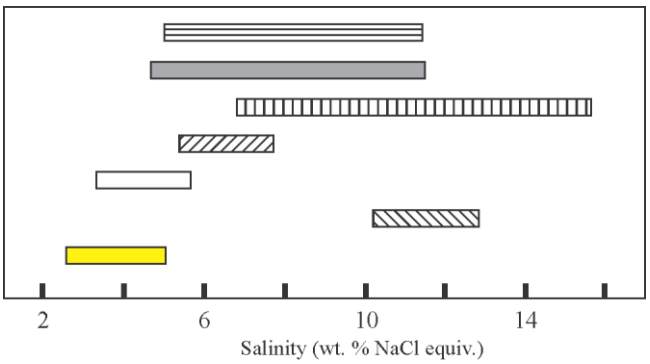

957

958 Fig (9)

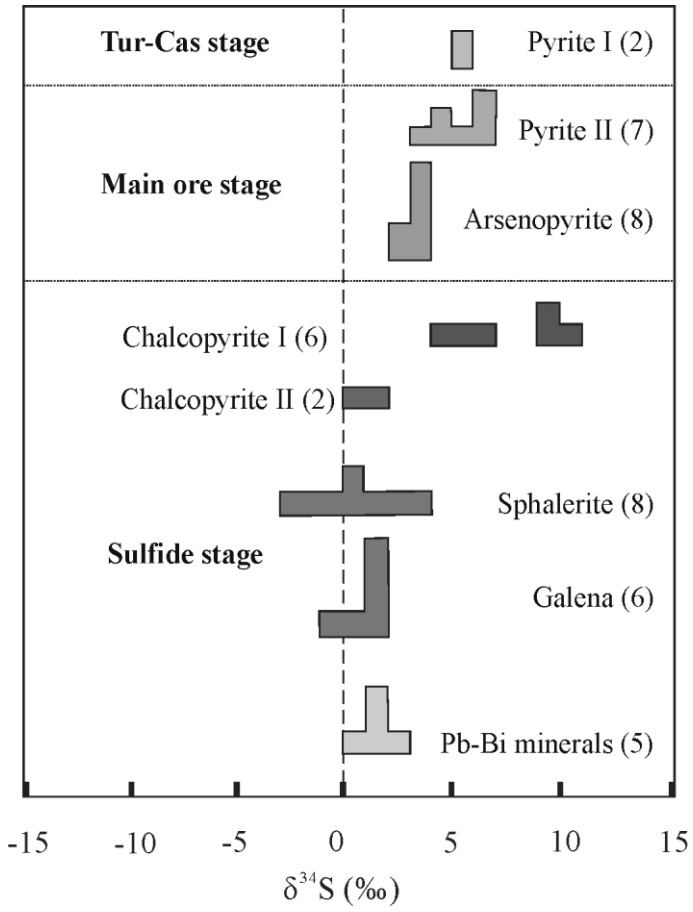

959

960 Fig (10)

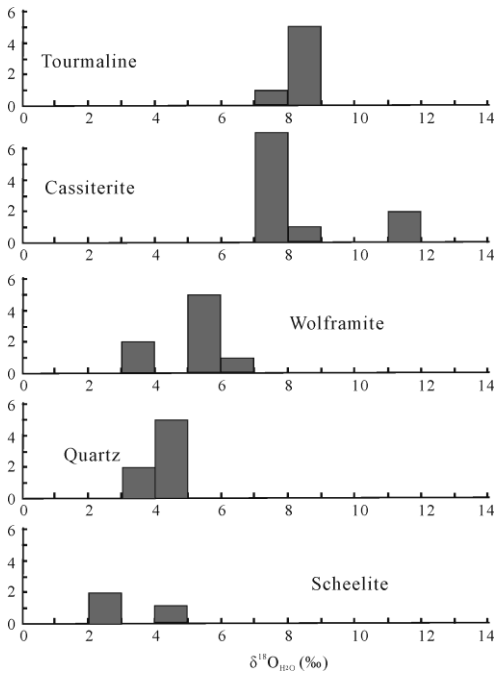

961

962 Fig (11)

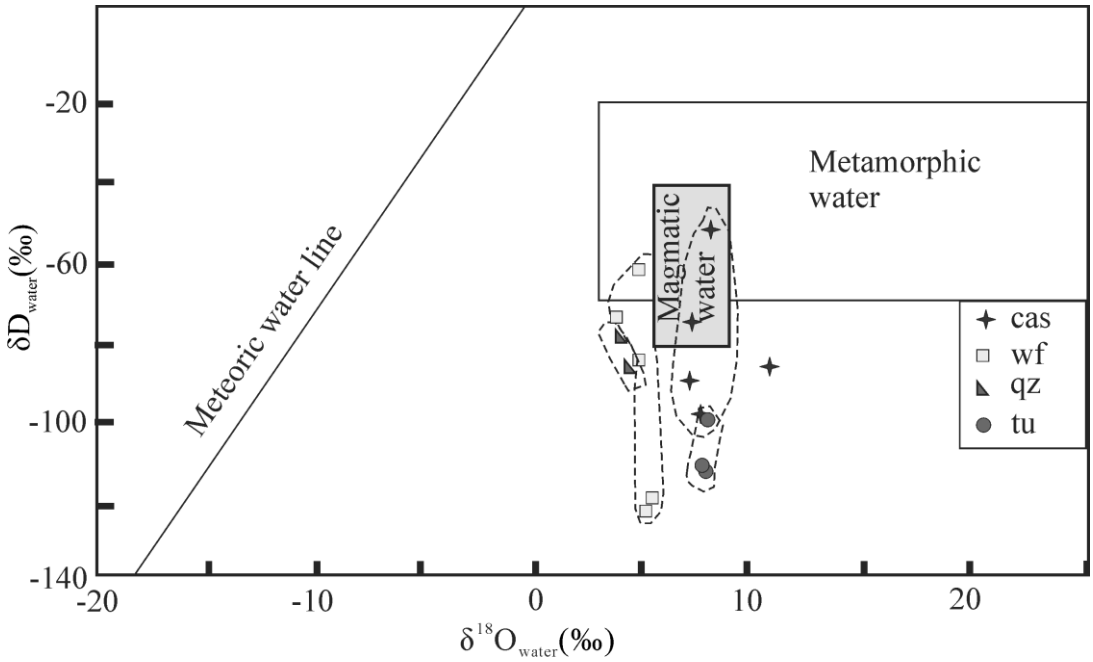

963

964 Fig (12)